Proceedings of the

SEVENTEENTH SYMPOSIUM ON ENERGY ENGINEERING SCIENCES

May 13-14, 1999

ARGONNE NATIONAL LABORATORY

Argonne, Illinois

Cosponsored by

Office of Basic Energy Sciences
U.S. DEPARTMENT OF ENERGY

and

Energy Technology Division
ARGONNE NATIONAL LABORATORY

Coordinated by

Argonne National Laboratory
9700 South Cass Avenue
Argonne, Illinois 60439

SEVENTEENTH SYMPOSIUM ON ENERGY ENGINEERING SCIENCES

FOREWORD

This Proceedings Volume includes the technical papers that were presented during the Seventeenth Symposium on Energy Engineering Sciences on May 13-14, 1999, at Argonne National Laboratory, Argonne, Illinois. The Symposium was structured into seven technical sessions, which included 25 individual presentations followed by discussion and interaction with the audience. A list of participants is appended to this volume.

The DOE Office of Basic Energy Sciences (BES), of which Engineering Research is a component program, is responsible for the long-term, mission-oriented research in the Department. The Office has prime responsibility for establishing the basic scientific foundation upon which the Nation's future energy options will be identified, developed, and built. BES is committed to the generation of new knowledge necessary to solve present and future problems regarding energy exploration, production, conversion, and utilization, while maintaining respect for the environment.

Consistent with DOE/BES mission, the Engineering Research Program is charged with the identification, initiation, and management of fundamental research on broad, generic topics addressing energy-related engineering problems. Its stated goals are to improve and extend the body of knowledge underlying current engineering practice so as to create new options for enhancing energy savings and production, prolonging the useful life of energy-related structures and equipment, and developing advanced manufacturing technologies and materials processing. The program emphasis is on reducing costs through improved industrial production and performance and expanding the nation's store of fundamental knowledge for solving anticipated and unforeseen engineering problems in energy technologies.

To achieve these goals, the Engineering Research Program supports approximately 130 research projects covering a broad spectrum of topics that cut across traditional engineering disciplines. The program focuses on three areas: (1) mechanical sciences, (2) control systems and instrumentation, and (3) engineering data and analysis. The Seventeenth Symposium involved approximately one-fourth of the research projects currently sponsored by DOE/BES Engineering Research Program.

The Seventeenth Symposium was held under the joint sponsorship of the DOE Office of Basic Energy Sciences and Argonne National Laboratory (ANL). Ms. Marianne Adair and Ms. Judy Benigno of ANL Conference Services handled local arrangements. Ms. Gloria Griparis of ANL's Information and Publishing Division, Technical Communication Services was responsible for assembling these proceedings and attending to their publication.

I am grateful to all that contributed to the success of the program, particularly to the participants for their excellent presentations and active involvement in discussions. The resulting interactions made the symposium a most stimulating and enjoyable experience.

Bassem F. Armaly, ER-15
Division of Engineering and Geosciences
Office of Basic Energy Sciences.

Proceedings of the

SEVENTEENTH SYMPOSIUM ON ENERGY ENGINEERING SCIENCES

May 13-14, 1999

Argonne National Laboratory

Argonne, Illinois

TABLE OF CONTENTS

Technical Session VI — Materials and Liquids

Technical Session VII — Multiphase Flow

REPRESENTING RANDOM FIELDS WITH BIORTHOGONAL WAVELETS

P. D. Spanos
L.B.Ryon Chair in Engineering

V. R. Rao
Graduate Student

Department of Mechanical Engineering,
Rice University, Houston, TX 77005

ABSTRACT

A new method of representing random fields in a biorthogonal wavelet basis is introduced. It is shown that a biorthogonal basis leads to an efficient representation of the random process with weakly correlated wavelet coefficients. This is tantamount to an increase in decorrelation capacity of the underlying basis functions. This increase is shown to result from the use of a smaller number of filter coefficients as compared to the Daubechies orthonormal family of wavelets.

INTRODUCTION

Recent developments in applied mathematics and signal processing have led to the development of wavelet theory and its application to problems of engineering interest. Some recent applications include the development of efficient algorithms for image processing and damage detection, for an exhaustive review, see [9]. The discovery of a class of compactly supported wavelets by Daubechies [6] was largely responsible for renewed interest of the engineering community in these functions. Daubechies wavelets can be used to approximate functions with desired accuracy using only a few significant coefficients. This [12] makes them ideal candidates for application to problems of engineering interest [1].

It is well known that second order random processes with a positive definite covariance matrix can be represented by means of a Karhunen-Loeve expansion. This expansion makes use of the eigenfunctions of the covariance kernel and results in a whitened representation by the use of uncorrelated random variables [7]. Wavelets however, are not the eigenfunctions of any operator

1

and hence cannot fully diagonalize the covariance matrix. They can however, be used to develop an approximate KL-expansion that results in a nearly diagonal covariance matrix.

In this context, wavelets have been shown to lead to efficient represention of stochastic processes and random fields [11, 13]. A wavelet-based KL-like expansion for wide-sense stationary random processes has been developed by Zhang and Walter in [16], where it is shown that the covariance kernel of a wide-sense stationary random process can be diagonalized by a set of biorthogonal wavelet bases obtained by starting with the Meyer wavelet. However, the resultant scaling function and wavelet are not compactly supported in the spatial domain.

The efficacy of algorithms used to represent random processes is crucial to many problems in stochastic mechanics. Conventional methods such as Monte-Carlo, Perturbation, and Neumann depend extensively on such represèntation schemes to simulate the behavior of the systems characterized by uncertainty. This is often a computationally expensive task, owing to the covariance structure of the random field. The computational complexity can be reduced to some extent by using the KL-expansion, as in the case of Stochastic Finite Element Method [7], where only uncorrelated random numbers need be used.

Potential applications of this study range from stochastic problems in structural mechanics [7], fluid mechanics [5], heat transfer [10], as well as other areas where parameter uncertainty is encountered [8]. While seeking a numerical solution to problems in these areas, it is desirable to have a solver that computes the solution to the governing partial differential equations in a wavelet domain, while taking into account the multiscale representation of the parameter uncertainty. In this paper, attention is focuses on the use of the biorthogonal spline wavelet basis to represent random processes, which could lead to the development of efficient solution schemes for a wide range of stochastic mechanics problems.

BIORTHOGONAL WAVELET BASES

Following the discovery of a class of compactly supported orthogonal wavelets by Daubechies [6], a generalization to biorthogonal wavelets was proposed by Cohen, Daubechies and Feauveau [3]. In the case of orthogonal wavelets, one set of filter coefficients $\{h_k\}$, for the scaling function and another set $\{g_k\}$ for the wavelets is sufficient to establish an orthogonal basis. In signal processing and filter-bank literature [12], these filters are referred to as the quadrature mirror filters that are used for both decomposition as well as synthesis. However, enforcing orthogonality of the wavelet and scaling function results in a loss of symmetry for the basis functions.

Compactly supported orthogonal wavelets can nearly diagonalize certain classes of differential operators [2]. It has been shown recently that biorthogonal wavelets built with orthogonal wavelets as a starting point [4] are also capable of diagonalizing a class of elliptic partial differential operators. Such operators arise in the numerical models of a number of engineering systems. The close parallels between the wavelet representation of operators [2] and second order statistics of random processes [15] raises the possibility of development of efficient biorthogonal wavelet schemes for problems in stochastic mechanics.

Extending the concepts of orthonormal wavelets [6] would require the introduction of dual MRA given by two sequences of nested subspaces V_j and $\tilde{V}_j$ such that

$$\{0\}\cdots \subset V_{-1} \subset V_0 \subset V_1 \subset \cdots L^2(\mathbb{R}), \qquad \{0\}\cdots \subset \tilde{V}_{-1} \subset \tilde{V}_0 \subset \tilde{V}_1 \subset \cdots L^2(\mathbb{R}). \tag{1}$$

The subspaces V_j and $\tilde{V}_j$ are spanned by translates of the primal and dual scaling functions at scale j, given by $\phi_{j,k}(x)$ and $\tilde{\phi}_{j,k}(x)$ respectively. The detail subspaces W_j and $\tilde{W}_j$ are spanned by the wavelet functions $\psi_{j,k}(x)$ and $\tilde{\psi}_{j,k}(x)$ respectively. The relations between the approximations and detail subspaces (primal and dual respectively) between any two successive scales is given by

$$V_{j+1} = V_j \oplus W_j \qquad \text{and} \qquad \tilde{V}_{j+1} = \tilde{V}_j \oplus \tilde{W}_j. \tag{2}$$

The bi-orthogonality of the primal and dual MRAs can be interpreted to imply the existence of refinement relations for the primal and dual functions $\phi(x)$, $\psi(x)$, $\tilde{\phi}(x)$ and $\tilde{\psi}(x)$, given by

$$\phi(x) = \sqrt{2}\sum_k h_k\, \phi(2x-k), \qquad \tilde{\phi}(x) = \sqrt{2}\sum_k \tilde{h}_k\, \tilde{\phi}(2x-k), \tag{3}$$

$$\psi(x) = \sqrt{2}\sum_k g_k\, \phi(2x-k), \qquad \tilde{\psi}(x) = \sqrt{2}\sum_k \tilde{g}_k\, \tilde{\phi}(2x-k), \tag{4}$$

The wavelet filter coefficients $\{g_k\}$ and $\{\tilde{g}_k\}$ are then given by

$$g_k = (-1)^k \tilde{h}_{\widetilde{M}-k-1}, \qquad \text{and,} \qquad \tilde{g}_k = (-1)^k h_{M-k-1}. \tag{5}$$

where M and $\widetilde{M}$ are the lengths of the primal and dual scaling filters $\{h_k\}$ and $\{\tilde{h}_k\}$ respectively. We note that for the case of orthogonal wavelets, the dual basis comprising of $\{\tilde{\phi}_{j,k}, \tilde{\psi}_{j,k}\}$ is the same as the primal basis.

The refinement relations in Eq. (3) - Eq. (4) can be written in the Fourier domain using the biorthogonal filter functions as

$$\hat{\phi}(2\omega) = m_0(\omega)\hat{\phi}(\omega), \qquad \hat{\tilde{\phi}}(2\omega) = \tilde{m}_0(\omega)\hat{\tilde{\phi}}(\omega), \tag{6}$$

$$\hat{\psi}(2\omega) = m_1(\omega)\hat{\phi}(\omega), \qquad \hat{\tilde{\psi}}(2\omega) = \tilde{m}_1(\omega)\hat{\tilde{\phi}}(\omega), \tag{7}$$

where, the filter refinement functions $m_0(\omega)$, $m_1(\omega)$ and their dual counterparts are given as

$$m_0(\omega) = \frac{1}{\sqrt{2}}\sum_k h_k\, e^{-i\omega k}, \qquad \tilde{m}_0(\omega) = \frac{1}{\sqrt{2}}\sum_k \tilde{h}_k\, e^{-i\omega k}, \tag{8}$$

$$m_1(\omega) = e^{i\omega}\overline{\tilde{m}_0(\omega+\pi)}, \qquad \tilde{m}_1(\omega) = e^{i\omega}\overline{m_0(\omega+\pi)}. \tag{9}$$

By virtue of the bi-orthogonality of the primal and dual subspaces, the basis functions satisfy

$$\langle \psi_{j,k}, \tilde{\psi}_{i,l} \rangle = \delta_{ji}\delta_{kl}, \qquad \langle \phi_{j,k}, \tilde{\psi}_{i,l} \rangle = 0, \tag{10}$$

$$\langle \phi_{j,k}, \tilde{\phi}_{i,l} \rangle = \delta_{ji}\delta_{kl}, \qquad \langle \tilde{\phi}_{j,k}, \psi_{i,l} \rangle = 0. \tag{11}$$

BIORTHOGONAL WAVELET TRANSFORM

The biorthogonal wavelet transform is similar to the discrete wavelet transform of orthonormal wavelets. Since the primal and dual basis functions constitute a basis in $L^2(I\!R)$, $f(x)$ can be represented as

$$f(x) = \sum_{j,k} d_k^j\, \psi_{j,k}(x) = \sum_{j,k} \tilde{d}_k^j\, \tilde{\psi}_{j,k}(x) \tag{12}$$

where the detail coefficients d_k^j and d_k^j are the projection of the function $f(x)$ onto the dual and primal biorthogonal bases respectively. The detail coefficients as well as the corresponding approximation coefficients are then given as

$$c_k^j = \langle f, \tilde{\phi}_{j,k} \rangle = \int f(x)\tilde{\phi}_{j,k}dx, \qquad d_k^j = \langle f, \tilde{\psi}_{j,k} \rangle = \int f(x)\tilde{\psi}_{j,k}dx, \tag{13}$$

$$\tilde{c}_k^j = \langle f, \phi_{j,k} \rangle = \int f(x)\phi_{j,k}dx, \qquad \tilde{d}_k^j = \langle f, \psi_{j,k} \rangle = \int f(x)\psi_{j,k}dx. \tag{14}$$

where,

$$\phi_{j,k}(x) = \sum_n h_{n-2k}\phi_{j+1,n}(x) \qquad \psi_{j,k}(x) = \sum_n g_{n-2k}\phi_{j+1,n}(x), \tag{15}$$

$$\tilde{\phi}_{j,k}(x) = \sum_n \tilde{h}_{n-2k}\tilde{\phi}_{j+1,n}(x) \qquad \tilde{\psi}_{j,k}(x) = \sum_n \tilde{g}_{n-2k}\tilde{\phi}_{j+1,n}(x) \tag{16}$$

These equations relate the basis functions on the fine scale to those at a coarser scale. The inverse relations where the fine scale coefficients are built from the coarse scale are given by

$$\phi_{j+1,k} = \sum_n \tilde{h}_{n-2k}\phi_{j,n} + \sum_n \tilde{g}_{n-2k}\psi_{j,n}, \qquad \tilde{\phi}_{j+1,k} = \sum_n h_{n-2k}\tilde{\phi}_{j,n} + \sum_n g_{n-2k}\tilde{\psi}_{j,n}. \tag{17}$$

The reconstruction in the case of an orthogonal wavelet basis involves only one set of functions. In the case of biorthogonal wavelets however, as the regularity of primal functions can be chosen to an an arbitrary degree, they are used in the reconstruction phase. The dual basis is used to carry out the decomposition into the coefficients c_k^j and d_k^j. This is due to the fact that while the primal functions are smoother, the dual functions possess more oscillations and are less regular. On the other hand, using the smoother primal basis for the decomposition and the dual basis for reconstruction has marked disadvantages. First, the smoother primal functions would result in a slow decay of the coefficients. Secondly, the function reconstructed with dual wavelets would be of low regularity. The projection is therefore carried on to a basis spanned by the dual functions $\{\tilde{\phi}_{j,k}(x)\}$ and $\{\tilde{\psi}_{j,k}(x)\}$ to obtain the approximation and detail coefficients. Reconstruction can then be carried out using these coefficients with the primal basis functions $\{\phi_{j,k}(x)\}$ and $\{\psi_{j,k}(x)\}$.

As a consequence of the imposed vanishing moments, the dual functions are more oscillatory in nature, and less regular than the primal functions. In particular, increased regularity of the

wavelet $\psi(x)$ requires additional vanishing moments for the dual wavelet function $\widetilde{\psi}(x)$. However, there need be no regularity conditions on $\widetilde{\psi}(x)$, which satisfies the relation

$$\int x^k \, \widetilde{\psi}(x) \, dx = 0, \qquad k = 0, 1, \ldots, M. \tag{18}$$

This is equivalent to requiring that the Fourier transform $\widetilde{m}_1(\omega)$ of the dual wavelet filter $\{\widetilde{g}_k\}$ have a zero of Mth order at $\omega = 0$, or that $m_0(\omega)$ be divisible by $(1 + e^{-i\omega})^M$.

The biorthogonal wavelet transform can be then obtained by substituting the refinement relations for $\widetilde{\phi}(x)$ and $\widetilde{\psi}(x)$ in Eq.(4) into Eq.(13) and Eq.(14). Then, a biorthogonal equivalent of the classical Mallat's Pyramidal algorithm for functional decomposition is obtained. Carrying out the above substitutions results in the following expressions for the coefficients c_k^j and d_k^j at scale j in terms of coefficients at the next finer scale $j + 1$.

$$c_k^j = \sum \widetilde{h}_{n-2k} \, c_n^{j+1}, \qquad \text{and} \qquad d_k^j = \sum \widetilde{g}_{n-2k} \, c_n^{j+1} \tag{19}$$

The complete biorthogonal wavelet transform of a function represented by N_f samples therefore involves successively decomposing each approximation vector $\mathbf{c}_j$, and is a $O(N_f)$ algorithm.

BIORTHOGONAL SPLINE WAVELETS

B-Splines, being analytically defined functions are ideal choice for wavelets when used to reconstruct functions. However, while B-splines of order n are refinable, their translates do not satisfy the orthonormality condition essential for their use as orthonormal basis functions. Cohen et al. [3] show that for any B-spline of order M, there exist many dual functions of order $\widetilde{M}$.

The scaling function $\phi(x)$ of a B-spline of order M can be obtained by repeated convolutions of the box-function on $[0, 1]$. Alternatively, the Mth derivative of $\phi(x)$ is defined by a series of the Fourier transform of its corresponding filter coefficients as

$$m_0(2\omega) = e^{-i\kappa\omega} \, (\cos\omega)^M, \tag{20}$$

where, $\kappa = 0$ for M even, and 1 for M odd. This is due to the fact that for M even, the primal and dual scaling functions, $\phi(x)$ and $\widetilde{\phi}(x)$ are symmetric about $x = 0$, while those for M odd are symmetric about $x = 1/2$. The corresponding wavelets $\psi(x)$ and $\widetilde{\psi}(x)$ are always centered about $x = 1/2$ and are symmetric for M even, antisymmetric for M odd. The dual scaling filter $\widetilde{m}_0(\omega)$ corresponding to the frequency response of the filter $\{\widetilde{h}_k\}$ is given by the equation

$$\widetilde{m}_0(2\omega) = e^{-i\kappa\omega} \, (\cos\omega)^{\widetilde{M}} \sum_{n=0}^{K-1} C_n^{K-1+n} \, (\sin\omega)^{2n}. \tag{21}$$

For a given primal scaling function of order M and dual scaling function of order $\widetilde{M}$, there can be many dual wavelet functions, all of which satisfy the condition $M + \widetilde{M} = 2K$, such that $\widetilde{M} \geq 1$. This condition is related to the symmetry that is retained by the biorthogonal basis functions, a property lacked by Daubechies wavelets.

RANDOM FIELD REPRESENTATION

The expressions for the second order statistics of the scaling function and wavelet coefficients have been discussed at length in [15] for the case of Daubechies wavelets. The goal of this section is to investigate the decay of the wavelet coefficients in a biorthogonal basis. These correlations between approximation coefficients c_k^j and detail coefficients d_k^j assuming that the dual functions are used to carry out the representation, are given by the following three relations

$$r_{k,l}^{j,j} = \int\int R_f(x_1,x_2)\tilde{\psi}_{j,k}(x_1)\tilde{\psi}_{j,l}(x_2)dx_1dx_2 = \sum_{m,n}\tilde{g}_m\,\tilde{g}_n\,a_{m+2k,n+2l}^{j+1,j+1} \tag{22}$$

$$b_{k,l}^{j,m} = \int\int R_f(x_1,x_2)\tilde{\phi}_{j,k}(x_1)\tilde{\psi}_{j,l}(x_2)dx_1dx_2 = \sum_{m,n}\tilde{g}_m\,\tilde{h}_n\,a_{m+2k,n+2l}^{j+1,j+1} \tag{23}$$

$$a_{k,l}^{j,m} = \int\int R_f(x_1,x_2)\tilde{\phi}_{j,k}(x_1)\tilde{\phi}_{j,l}(x_2)dx_1dx_2 = \sum_{m,n}\tilde{h}_m\,\tilde{h}_n\,a_{m+2k,n+2l}^{j+1,j+1} \tag{24}$$

The above integrals can be evaluated recursively using the refinement relations for $\tilde{\phi}(x)$ and $\tilde{\psi}(x)$ in Eq.(3) and (4). These integrals then can be evaluated in $O(N\log N)$ and $O(N)$ operations for non-stationary and stationary processes respectively as shown in [15]. Further speedup can be obtained when coiflets with vanishing moments equally distributed between the scaling function and wavelet are used, resulting in $O(N)$ operational algorithms in the case of non-stationary processes. However, since the support for the coiflets increases with additional vanishing moments imposed on the scaling function, the increase in speedup is offset by increasing filter lengths. (Coiflets with M vanishing moments on the wavelet and $M-1$ moments for the scaling function have a support length $6M-1$, as opposed to $2M-1$ for an equivalent Daubechies wavelet with M vanishing moments.)

VARIANCE OF WAVELET COEFFICIENTS

The expressions for the variance of wavelet coefficient correlations can be derived from the relations in Eqs. (22) to Eq.(24) by using the appropriate refinement relations for the dual functions. In particular, we look at at the correlation of the scaling function coefficients $a_{k,l}^{j,j}$, given in Eq.(24). This equation can be rewritten using the moments of the dual scaling function by making a change of variable $y_i = x_i - 2^{-j}k,\quad i = 1,2$, and then expanding the autocorrelation function about $(y_1,y_2) = 2^{-j}(k,l)$. This yields the following expansion, assuming that that the autocorrelation function is atleast Q times differentiable.

$$a_{k,l}^{j,j} = 2^j\int\int\left[R_f(2^{-j}k,2^{-j}l) + \sum_{n=1}^{Q}\sum_{i=0}^{n}\frac{1}{n!}R_{n,i}x_1^i x_2^{n-i}\right]\tilde{\phi}(2^j x_1)\tilde{\phi}(2^j x_2)dx_1dx_2 \tag{25}$$

where,

$$R_{n,i} = \left.\frac{\partial^n R_f(x_1,x_2)}{\partial^i x_1\partial^{n-i}x_2}\right|_{(x_1=2^{-j}k,x_2=2^{-j}l)} \tag{26}$$

For sufficiently large j, or in other words, for a fine enough scale, the leading term dominates all other terms by a factor of 2^{-j}, owing to the normality of the dual functions. Hence

$$a_{k,l}^{j,j} \approx 2^{-j} R_f(2^{-j}k, 2^{-j}l). \tag{27}$$

Carrying out a similar exercise with the dual wavelet (with M vanishing moments such that $M \geq Q$) for the correlation coefficients $r_{k,l}^{j,j}$ leads to the result that

$$r_{k,l}^{j,j} \approx C2^{-j(Q+1)}, \quad \text{and hence} \quad \frac{r_{k,l}^{j,j}}{a_{k,l}^{j,j}} \approx C2^{-jQ}. \tag{28}$$

Note that the nature of the above ratio is the same as obtained for Daubechies Wavelets representation of random processes [14]. However, the dual basis offers more flexibility due to the relaxation of the condition of orthonormality.

CROSS-SCALE CORRELATIONS

The cross-scale correlations for the general case of non-stationary random processes can be computed using the expressions in Eqs.(22) to (24). It is possible to obtain upper bounds for these coefficients in the the case of stationary random processes, In particular, it can be shown that the cross-scale correlation obtained from low order splines shows a decay which is better than that obtained with high order Daubechies wavelets. This decay is related to the function $\chi_k(\omega)$, given by the equation

$$\chi_k(\omega) = 2^{-j/2+2} |\tilde{m}_1(\omega)|.|\tilde{m}_1(2^k\omega)|. \prod_{j=0}^{k-1} |\tilde{m}_0(2^j\omega)| \tag{29}$$

An upper bound for cross-scale correlation of wavelet coefficients is given by the relation

$$\left| r_{k,l}^{j,m} \right| \leq max(S(\omega)) \int_0^\pi \chi_{|j-m|}(\omega), \tag{30}$$

It is evident from the above equations that the function $\chi_k(\omega)$ determines to a large extent the magnitude of $r_{k,l}^{j,m}$ across scales. Therefore, $\chi_k(\omega)$ will hereafter be referred to as the de-correlation function.

CONCLUSIONS

Based on the studies carried out in the preceding sections, it may be surmised that biorthogonal wavelets are better than Daubechies orthogonal wavelets in representing random fields. This is due to the increased de-correlation capacity of the dual wavelets in a biorthogonal basis. It has been found that increasing the number of vanishing moments on the dual wavelet lead to a faster decay of the wavelet correlation across scales through attenuation of the peaks of the function $\chi_k(\omega)$ in Eq.(29). It has also been observed that for a given order of the primal wavelet, there is a limiting

order of the dual wavelet beyond which the correlation cannot be weakened any further. This is due to the fact that for increasing order of the dual wavelet, the basis functions become smoother without any further qualitative changes in their appearance. Hence their approximation properties change only marginally. This feature is also reflected in the variance of the resulting wavelet and scaling functions across scales, which is nearly the same for wavelets of increasing dual order. This implies that a low order dual wavelet can be adequate for representing the random process if the tolerance levels on the correlation across scales are not too strict.

The de-correlation function defined in Eq.(29) is shown in Fig. for Daubechies wavelets with $M = 1$ (Haar wavelets) and for Biorthogonal wavelets with $M = 1$, $\widetilde{M} = 5$. It can be seen from these figures that the cross-scale correlation will decay faster in the biorthogonal case, in light of Eq.(30). This decay can be attributed to the attenuation of trailing hills of the de-correlation function in $\omega \in [0 \ \pi]$.
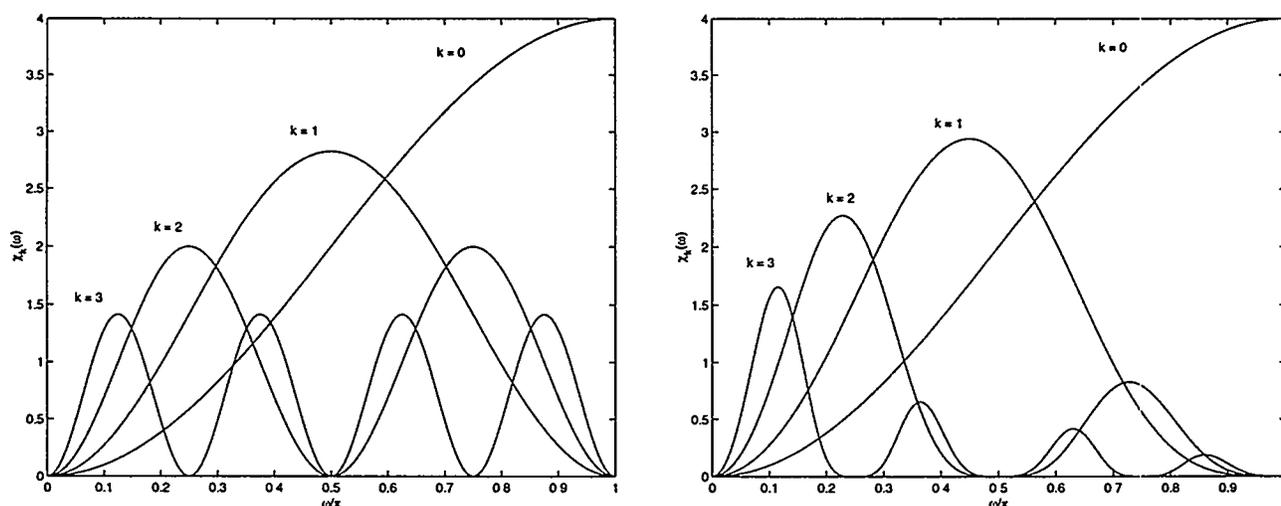
Figure 1: De-correlation function from Daubechies wavelets ($M = 1$) versus Bi-orthogonal wavelets ($M = 1$, $\widetilde{M} = 5$). Tne number of scales used is given by k.

References

[1] K. Amaratunga, J.R. Williams, S. Qian, and J. Weiss. Wavelet-galerkin solutions for one-dimensional partial differential equations. *Int. J. Num. Meth. Eng.*, 27:2703–2716, 1994.

[2] G. Beylkin. On the representation of operators in bases of compactly supported wavelets. *SIAM Journal of Numerical Analysis*, 6(6):1716–1740, 1993.

[3] A. Cohen, I. Daubechies, and J.-C. Feauveau. Biorthogonal bases of compactly supported wavelets. *Comm. Pure and Appl. Math.*, 45:485–560, 1992.

[4] S. Dahlke and I. Weinreich. Wavelet-Galerkin methods: An adapted biorthogonal wavelet basis. *Constructive Approximation*, 9:237–262, 1993.

[5] M.P. Dainton, M.H. Goldwater, and N.K. Nichols. Direct computation of stochastic flow in reservoirs with uncertain parameters. *Journal of Computational Physics*, 130:203–216, 1997.

[6] I. Daubechies. Orthonormal bases of compactly supported wavelets. *Comm. Pure and Appl. Math.*, 41:909–996, 1988.

[7] R. G. Ghanem and P. D. Spanos. *Stochastic Finite Elements: A Spectral Approach.* Springer-Verlag, 1991.

[8] J. Glimm and D. Sharp. Stochastic partial differential equations: Selected applications in continuum physics. Technical Report Preprint # SUNYSB-AMD-96-24, University of Stony Brook, Stony Brook, NY 11794, 1996.

[9] B. Jawerth and W. Sweldens. An overview of wavelet based multiresolution analyses. *SIAM Rev.*, 36(3):377–412, 1994.

[10] G. D. Manolis and R. P. Shaw. Boundary integral formulation for 2D and 3D thermal problems exhibiting a linearly varying stochastic conductivity. *Computational Mechanics*, 17:406–417, 1996.

[11] P.D. Spanos and B.A. Zeldin. Wavelets concepts in stochastic mechanics. *Submitted to Probabilistic Engineering Mechanics*, 1997. Preprint, Department of Mechanical Engineering, Rice University.

[12] G. Strang and T. Nguyen. *Wavelets and Filterbanks.* Wellesley-Cambridge Press, 1996.

[13] P.W. Wong. Wavelet decomposition of harmonizable random processes. *IEEE Trans. Information Theory*, 39(1):7–18, January 1993.

[14] B. A. Zeldin and P. D. Spanos. Random field representation and synthesis using wavelet bases. *Trans. ASME Journal of Applied Mechanics*, 63:946–952, 1996.

[15] B.A. Zeldin. *Representation and synthesis of random fields : ARMA, Galerkin, and wavelet procedures.* PhD thesis, Rice University, Houston, Texas, 1996.

[16] J. Zhang and G. Walter. A wavelet-based KL-like expansion for wide-sense stationary random processes. *IEEE Trans. on Signal Processing*, 42:1737–1745, 1994.

NONLINEAR DIFFUSION AND THE PREISACH MODEL OF HYSTERESIS

I.D. Mayergoyz

Electrical Engineering Department
University of Maryland, College Park, MD 20742

ABSTRACT

It is shown that, in the case of abrupt (sharp) magnetic transitions, eddy current hysteresis can be represented in terms of the classical Preisach model. In this representation, memory effects are taken into account by the structure of the Preisach model, while dynamic effects are accounted for by a special form of the input to the model. A startling consequence of this representation is the fact that nonlinear dynamic eddy current hysteresis can be fully characterized by its step response.

INTRODUCTION

Consider a conducting magnetic cylinder of arbitrary cross-section. Suppose that this cylinder is subject to time varying uniform magnetic field $H_0(t)$, whose direction is parallel to the side boundary of the cylinder (see Figure 1). That magnetic field induces eddy currents in the cylinder, which are described by the following nonlinear diffusion equation:

$$\nabla^2 H = \sigma \frac{\partial B(H)}{\partial t}, \tag{1}$$

where all symbols have their usual meaning.
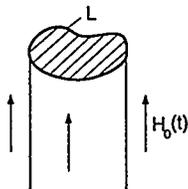
Figure 1

Let $\phi(t)$ be the magnetic flux through the cylinder, and consider the relation (mapping) between the magnetic field $H_0(t)$ at the cylinder boundary and $\phi(t)$. It is

well known that this relation exhibits rate-dependent (dynamic) hysteresis. It is the goal of this paper to demonstrate that, in the case of the sharp magnetic transition

$$B(H) = B_m \text{ sign } H, \tag{2}$$

the above hysteretic relation can be represented in terms of the classical Preisach model.

TECHNICAL DISCUSSION

To start the discussion, let us assume that the initial value of the magnetic flux density in the cylinder is equal to $-B_m$. Let us also assume that $H_0(t)$ varies with time as it is shown in Figure 2. It is clear that during the time interval $0 < t < t_1$ a positive rectangular front of magnetic flux density is formed and it moves inwards until $H_0(t)$ remains positive. At time t_1, the motion of the positive rectangular front is terminated and a negative rectangular front of magnetic flux density is formed. During the time interval $t_1 < t < t_2$, the latter front extends inwards and its motion is terminated at time t_2. At subsequent time intervals ($t_2 < t < t_3, t_3 < t < t_4, t_4 < t < t_5$, etc.) new positive and negative rectangular fronts are formed and they progress inwards by partially
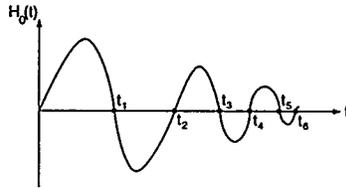
Figure 2

(or completely) wiping out the previous fronts. Next, we shall transform nonlinear diffusion equation (1)-(2) to rate independent forms for "odd" ($t_{2k} < t < t_{2k+1}$) and "even" ($t_{2k-1} < t < t_{2k}$) time intervals, respectively. During "odd" time intervals, $H_0(t) > 0$ and positive fronts of the magnetic flux density are formed and they progress inwards. By introducing the function

$$w_{2k+1}^+ = \int_{t_{2k}}^t H(\tau)d\tau, \quad \left(H(t) = \frac{\partial w_{2k}^+}{\partial t}\right), \tag{3}$$

by integrating equation (1) with respect to time from t_{2k} to t and by using formula (2), we derive:

$$\nabla^2 w_{2k+1}^+ = \sigma \left[B_m \text{ sign } \left(\frac{\partial w_{2k}^+}{\partial t}\right) - B(t_{2k})\right]. \tag{4}$$

The last equation is valid within the region $\Omega_{2k+1}^+(t)$ occupied by a newly formed positive front. In this region, function w_{2k}^+ is monotonically increased with time and,

consequently, sign $\left(\frac{\partial w_{2k}^+}{\partial t}\right) = 1$. In the same region, we also have $B(t_{2k}) = -B_m$. As a result, equation (4) takes the form of the Poisson equation:

$$\nabla^2 w_{2k+1}^+ = 2\sigma B_m \tag{5}$$

The solution of the last equation is subject to the following boundary conditions:

$$w_{2k+1}^+(t)|_L = w_{0,2k+1}^+(t) = \int_{t_{2k}}^t H_0(\tau)d\tau, \tag{6}$$

$$w_{2k+1}^+(t)|_{L_{2k+1}^+(t)} = 0, \tag{7}$$

$$\frac{\partial w_{2k+1}^+}{\partial \nu}|_{L_{2k+1}^+(t)} = 0, \tag{8}$$

where ν is a normal to the moving boundary $L_{2k+1}^+(t)$ of the region $\Omega_{2k+1}^+(t)$.

Boundary conditions (7) and (8) at the moving boundary $L_{2k+1}^+(t)$ follow from the fact that magnetic field and tangential component of electric field are equal to zero at the points of $L_{2k+1}^+(t)$ for the time interval $t_{2k} < \tau < t$, that is, before the arrival of the positive front.

During "even" time intervals, $H_0(t) < 0$ and negative fronts of the magnetic flux density are formed and they extend inwards with time. By introducing the function

$$w_{2k}^- = \int_{t_{2k-1}}^t H(\tau)d\tau, \tag{9}$$

and by literally repeating the same line of reasoning as before, we end up with the following boundary value problem:

$$\nabla^2 w_{2k}^- = -2\sigma B_m, \tag{10}$$

$$w_{2k}^-(t)|_L = w_{0,2k}(t) = \int_{t_{2k-1}}^t H_0(\tau)d\tau, \tag{11}$$

$$w_{2k}^-(t)|_{L_{2k}^-(t)} = 0, \tag{12}$$

$$\frac{\partial w_{2k}^-}{\partial \nu}|_{L_{2k}^-(t)} = 0. \tag{13}$$

The following properties can be inferred by inspecting boundary-value problems (5)-(8) and (10)-(13).

Rate Independence Property.

Boundary value problems (5)-(8) and (10-13) are rate independent. Consequently, the instantaneous positions and shapes of moving boundaries $L_{2k+1}^+(t)$ and $L_{2k}^-(t)$ are determined by instantaneous boundary values of $w_{0,2k+1}^+(t)$ and $w_{0,2k}^-(t)$, respectively.

Symmetry Property.

Boundary value problems (5)-(8) and (10)-(13) have identical (up to a sign) mathematical structures. This suggests that, if $|w_{0,2k}^-| = |w_{0,2k+1}^+|$, then the corresponding boundaries L_{2k}^- and L_{2k+1}^+ are identical. In other words, there is complete **symmetry** between inward motions of positive and negative fronts.

Now, we introduce the function:

$$w_0(t) = \int_0^t H_0(\tau)d\tau. \tag{14}$$

It is clear that function $w_0(t)$ is a sum of the appropriate functions $w_{0,2k}^+(t)$ and $w_{0,2k}^-(t)$. It is also clear that $w_0(t)$ achieves local maxima at $t = t_{2k+1}$ and local minima at $t = t_{2k}$. Next, we intend to show that $\phi(t)$ vs. $w_0(t)$ is a rate independent hysteretic relation. The rate independence of the above relation directly follows from the previously stated Rate Independence Property. It is also true that $\phi(t)$ vs. $w_0(t)$ is a hysteretic relation. Indeed, the current value of $\phi(t)$ depends not only on the current value of $w_0(t)$ but on the past extremum values of $w_0(t)$ as well. This is because the past extremum values of $w_0(t)$ determine the final locations and shapes of positive and negative rectangular fronts of B that were generated in the past. These past and motionless rectangular fronts affect the current values of $\phi(t)$. It is also apparent that there are reversals of $\phi(t)$ at extremum values of $w_0(t)$. In other words, new branches of ϕ vs. w_0 relation are formed after local extrema of $w_0(t)$. The previous discussion clearly suggest that ϕ vs. w_0 is a rate independent hysteretic relation. Next, we shall demonstrate that this hysteretic relation exhibits the wiping-out and congruency properties. Indeed, every monotonic increase (or decrease) of $w(t)$ results in the formation of a positive (or negative) rectangular front of the magnetic flux density, which extends inwards. This moving front will wipe out those previous rectangular fronts if they correspond to those previous extremum values of $w_0(t)$, which are exceeded by a new extremum value of $w_0(t)$. In this way, the effect of those previous extremum values of $w_0(t)$ on the future values of magnetic flux $\phi(t)$ is completely eliminated. This means that the wiping-out property holds [1]. Now, we shall demonstrate the validity of the congruency property. Consider two different boundary conditions: $w_0^{(1)}(t)$ and $w_0^{(2)}(t)$. Suppose that $w_0^{(1)}(t)$ and $w_0^{(1)}(t)$ have different past histories (different past extrema) but, starting from some instant of time, they vary monotonically back-and-forth between the same two extremum (reversal) values. It is apparent that the above back-and-borth variations of $w_0^{(1)}(t)$ and $w_0^{(2)}(t)$ will affect in the identical way the same surface layers of the conducting cylinder. Consequently, those variations will result in equal increments of the magnetic flux, which is tantamount to the congruency of the corresponding minor loops. Since the wiping-out and congruency properties constitute necessary and sufficient conditions for applicability of the Preisach model ([1],[2]), we conclude that the ϕ vs. w_0 relation can be represented by the Preisach model. As a result, we arrive

13

at the following representation of eddy current hysteresis:

$$\phi(t) = \iint\limits_{\alpha \geq \beta} \mu(\alpha, \beta) \hat{\gamma}_{\alpha\beta} \left(\int_0^t H_0(\tau) d\tau \right) d\alpha d\beta. \qquad (15)$$

It is worthwhile to stress two remarkable points related to the above result. First, memory effects and dynamic effects of eddy current hysteresis are clearly separated. The memory effects are taken into account by the structure of the Preisach model, while the dynamic effects are accounted for by the nature of the input $\left(\int_0^t H_0(\tau) d\tau \right)$ to this model. Second, the last formula suggests that the Preisach model can be useful for the description of hysteresis exhibited by spatially distributed systems. This is in contrast with the traditionally held point of view that the Preisach model describes only local hysteretic effects in magnetic materials.

Next, we turn to the discussion of properties of function $\mu(\alpha, \beta)$ in formula (15). By using the symmetry Property, it can be inferred **that the same increments of $w_0(t)$, occurred after different extremum values of $w_0(t)$, result in the same increments of $\phi(t)$.** This fact implies that the integral

$$F(\alpha, \beta) = \iint\limits_{T(\alpha,\beta)} \mu(\alpha', \beta') d\alpha' d\beta' \qquad (16)$$

over a triangle $T(\alpha, \beta)$, defined by inequalities $\alpha' < \alpha, \beta' > \beta, \alpha' - \beta' \geq 0$, does not depend on α and β separately but rather on the difference $\alpha - \beta$. In other words, the value of the above integral is invariant with respect to parallel translations of the triangle $T(\alpha, \beta)$ along the line $\alpha = \beta$. This is only possible if

$$\mu(\alpha, \beta) = \mu(\alpha - \beta). \qquad (17)$$

This means that function μ assumes constant values along the lines $\alpha - \beta$=const. By using formula (17), it can be established that function μ can be found by measuring only the ascending (or descending) branch of the major loop of ϕ vs. w_0 hysteretic nonlinearity. It can also be shown that any path traversed on (w_0, ϕ) plane is piecewise congruent to the ascending branch of the major loop. Thus, ϕ vs. w_0 hysteretic nonlinearity is completely characterized by the ascending branch of the major loop. This branch can be found experimentally by measuring the step response of eddy current hysteresis. Indeed, by assuming initial condition $B(0) = -B_m$ and by applying the field $H_0(t) = 1$, we can measure flux $\phi(t)$, which corresponds to $w_0(t) = t$. By excluding time t, we find the function $\phi(w_0)$, which describes the ascending branch of the major loop. Thus, we arrive at the remarkable conclusion that **nonlinear (and dynamic) eddy current hysteresis can be fully characterized by its step response.**

Formula (15) can be generalized to the case when abrupt (sharp) magnetic transitions are described by rectangular hysteresis loops (see Figure 3). It can be shown that in that case formula (15) can be modified as follows:

$$\phi(t) = \iint\limits_{\alpha \geq \beta} \mu(\alpha,\beta)\hat{\gamma}_{\alpha\beta} \left(\int_0^t \lambda(H_0(\tau))d\tau \right) d\alpha d\beta, \qquad (18)$$

where function $\lambda(H_0)$ is defined as:

$$\lambda(H_0) = (H_0 - H_c)s(H_0 - H_c) + (H_0 + H_c)s(-H_0 - H_c), \qquad (19)$$

and $s(\cdot)$ is the unit step function.

We conclude this paper with an elegant derivation of the formula for the front $z_0(t)$ in the case of plane boundary, that is in $1D$ case. In that case, the boundary-value problem (5)-(8) is reduced to:

$$\frac{d^2w}{dz^2} = 2\sigma B_m, \quad \text{if } 0 < z < z_0(t), \qquad (20)$$

$$w(0,t) = w_0(t) = \int_0^t H_0(\tau)d\tau, \qquad (21)$$

$$w(z_0(t),t) = 0, \quad \frac{dw(z,t)}{dz}\Big|_{z_0(t)} = 0. \qquad (22)$$
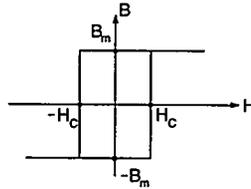
Figure 3

The solution to equation (20), which satisfies the boundary condition (21) and second boundary condition (22) is given by:

$$w(z,t) = \sigma B_m z^2 - 2\sigma B_m z z_0(t) + w_0(t). \qquad (23)$$

To find $z_0(t)$, we use the first boundary condition (22), which leads to:

$$-\sigma B_m z_0^2(t) + w_0(t) = 0. \qquad (24)$$

The last expression yields:

$$z_0(t) = \sqrt{\frac{w_0(t)}{\sigma B_m}} = \left(\frac{\int_0^t H_0(\tau)d\tau}{\sigma B_m} \right)^{\frac{1}{2}}. \qquad (25)$$

15

This is the well known formula that can be traced back to the paper of W. Wolman and H. Kaden [3].

ACKNOWLEDGEMENT

REFERENCES

1. I.D. Mayergoyz, "Mathematical Models of Hysteresis", New York, Springer-Verlag, 1991.

2. I.D. Mayergoyz, Phys. Rev. Let., **56**, No. 15, 1986, 1518-1521.

3. W. Wolman and H. Kaden, Z. Techn. Phys., **13**, 1932, 330-345.

TUNNELING CHARACTERISTICS AND LOW-FREQUENCY NOISE OF HIGH-T_c SUPERCONDUCTOR/NOBLE-METAL JUNCTIONS[1]

Yizi Xu and J. W. Ekin

National Institute of Standards and Technology
Boulder, Colorado 80303, U.S.A.

ABSTRACT

We report extensive measurements of transport characteristics and low-frequency resistance noise of c-axis YBCO/Au junctions. The dominant conduction mechanism is tunneling at low temperatures. The conductance characteristic is asymmetric, and the conductance minimum occurs at a non-zero voltage. These features can be qualitatively explained by modeling the YBCO/Au interface with a *Schottky* barrier. The model shows the YBCO surface behaves like a p-type semiconductor, with a Fermi degeneracy of about 0.1 eV. This is consistent with a carrier density of $3 \times 10^{21}\, cm^{-3}$, and a band mass of 2.6 times that of the free-electron mass. The barrier-height is approximately 1.0 eV. We show that interface states and disorder play an important role in determining the conductance characteristics. Low-frequency noise measurements of many junctions with contact areas ranging from $4\,\mu m^2$ to $64\,\mu m^2$, over a wide temperature and bias range, indicate that the noise figure for engineering design may be expressed as a normalized resistance fluctuation $\delta R/R \simeq 6 \times 10^{-4}/\sqrt{Hz}$ at 10 Hz.

INTRODUCTION

The YBCO/Au interface plays an important role in many high-T_c electronics applications. For example, the electrical and mechanical properties of this interface determine the integrity of Au wire-bond contacts to YBCO thin film devices, which determines the reliability of device packaging. In another application, YBCO thin films are used to make detection coils in low-field Magnetic Resonance Imaging (MRI) systems. The use of high-T_c superconductors offers increased signal-to-noise ratio, enabling low-field MRI systems. It is therefore very important that the contacts to the YBCO detection coils be both low-resistance and low-noise in order not to compromise the benefits of using these superconductors.

---

[1]Contribution of NIST, not subject to copyright.

17

The success of these applications requires an understanding of the physical mechanism of conduction across the YBCO/Au interface. The purpose of this work is to gain such an understanding. In this paper we first report our extensive measurements of transport characteristics of YBCO/Au junctions. We then present a simple model for our results. Finally we present low-frequency resistance noise data of our junctions, which are of important technological value and also provide insight for understanding YBCO/Au interfaces.

Fabrication and Conductance Measurement

The YBCO thin films used in this work were prepared using the pulsed laser deposition technique. The films were c-axis orientated, with T_c in the range of 87 to 91 K. We pattern our films using standard photolithography. One unique feature in our process is the use of an insulating layer of MgO to define small contact areas, which varied from $2 \times 2 \ \mu m^2$ to $16 \times 16 \ \mu m^2$. The current flows nominally along the c-axis of YBCO, through a native tunnel barrier, into the Au electrode. The native tunnel barrier was formed on the surface of the c-axis orientated YBCO film during the fabrication process, and is thought to consist of adsorbed impurities, as well as the degraded top-most atomic layers of the YBCO film. Electrically, the native tunnel barrier behaves as a thin insulating or semiconducting layer between the superconductor (YBCO) and normal metal (Au). The dominant conduction mechanism of such junctions is tunneling at low temperatures. The low-temperature tunneling resistance of our junctions with different areas ranged from a few ohms to a few hundred kilohms. We developed a system for measuring junction current vs. voltage characteristics and its first derivative with high resolution and data acquisition rate. The details of our junction fabrication and measurement techniques can be found elsewhere [1].

A typical low-temperature conductance vs. voltage curve for our junctions is shown in Fig. 1. Note that the curve is asymmetric: the incremental conductance (i.e., dI/dV) at a forward bias, when the Au-electrode is biased positively with respect to the YBCO-electrode, is greater than the corresponding reverse bias. The low bias range, shown in more detail in the inset, is characterized by the following features: (A) a zero-bias conductance peak, (B) for voltages less than about 30 mV the conductance is conspicuously lower than that extrapolated from the high bias range (the dashed line in the inset), (C) a conductance minimum at a reverse bias (V_{min} in the inset), which would be apparent if the features in (A) and (B) were suppressed.

There has been considerable controversy surrounding the issue of the zero-bias conductance peak (ZBCP) in YBCO/noble-metal junctions. The general consensus is that this is a result of d-wave paring symmetry in YBCO [2, 3, 4, 5]. The conductance reduction for bias below about 30 mV is due to the formation of the superconducting gap in YBCO, which had been extensively studied and well documented [6]. For our present purpose it suffices to say that both these features are associated with superconducting properties of YBCO. If we were able to suppress the onset of superconductivity in YBCO at low temperatures, then the conductance vs. voltage would have followed the dashed line in the inset of Fig. 1, showing a conductance minimum at a bias $V_{min} < 0$.

In order to show the systematic behavior of junction conductance vs. voltage characteristics, we plotted normalized conductances for several junctions in Fig. 2. Each curve is normalized by its conductance value at 100 mV. For the purpose of identification the junctions' zero-bias contact resistivities (in units of $\Omega \cdot cm^2$) and areas are listed in the same order as their zero-bias conductance peaks in the figure. For example, the curve with the highest zero-bias conductance peak corresponds to the first entry of the list.
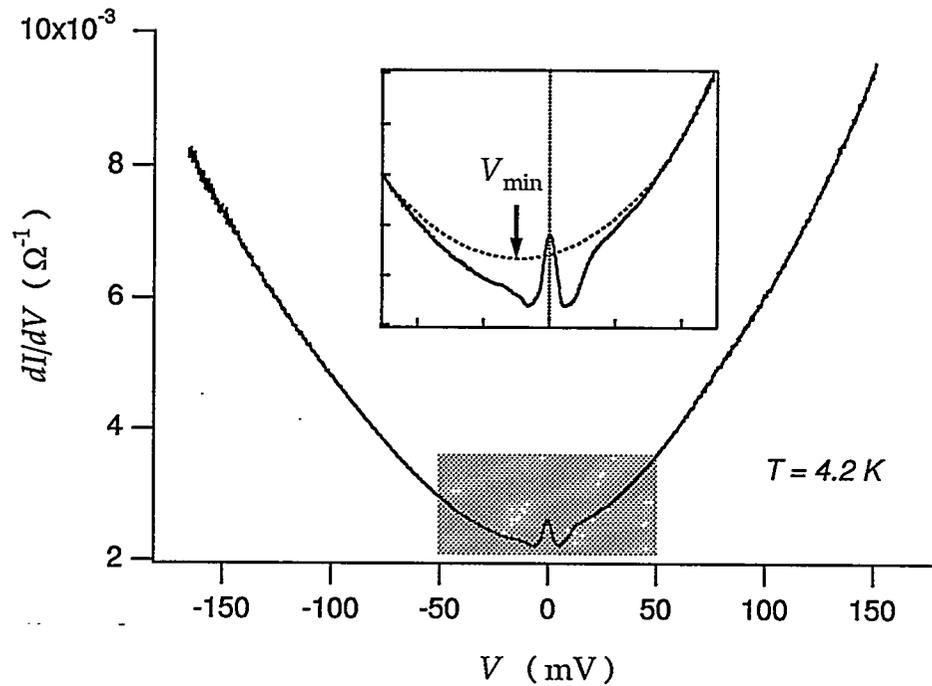
18

Figure 1: Conductance vs. voltage characteristics of a junction at 4.2 K. The low-bias region (shaded) is shown in more detail in the inset
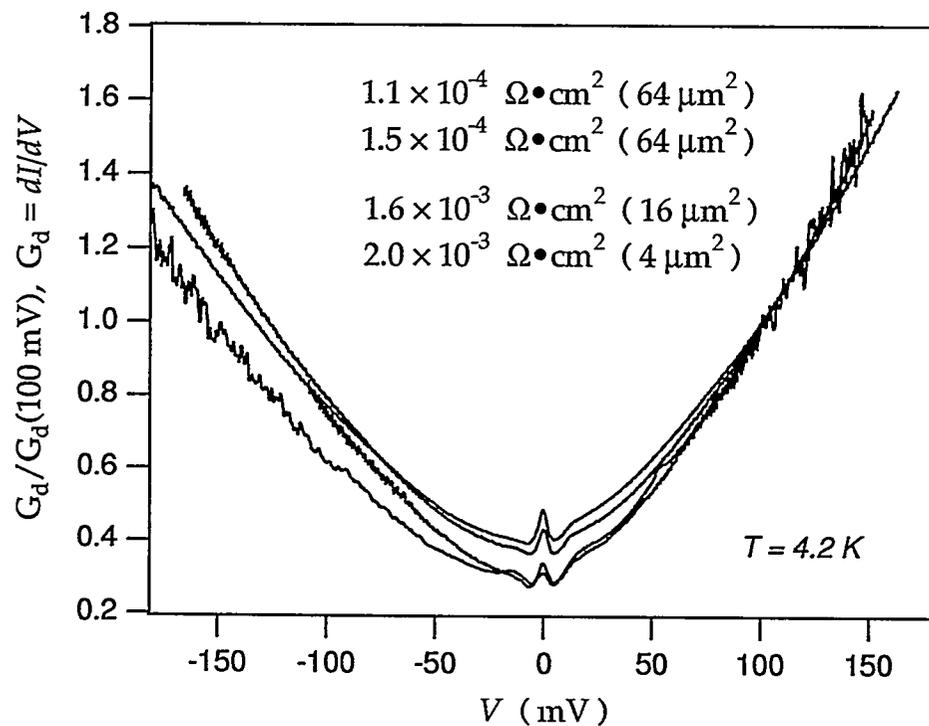

Figure 2: Systematic behavior of normalized junction conductance vs. bias voltage.

Despite the large range of junction area and contact resistivity, the normalized conductance vs. voltage curves are remarkably similar. In particular, the conductance asymmetry and a negative minimum-conductance voltage are general features. It follows that we should seek a physical model for this junction interface system which can explain these general features in conductance characteristics, and yet has a degree of flexibility to accommodate variations in individual junctions. The *Schottky-Barrier* model, which describes the interface between a semiconductor and a free-electron-like metal, is one such model.

<div align="center">THE Schottky-Barrier MODEL</div>

Fig. 3 depicts the basics of the *Schottky-Barrier* model. It shows electron potential profiles across the interface of a metal and an n-type degenerate semiconductor under different bias conditions.

The left panel shows the system under zero bias. The Fermi levels are at the same energy. The potential of the semiconductor conduction band at the interface is higher than its bulk value (band-bending). The band-bending extends over many atomic layers into the semiconductor, forming a potential barrier of height V_{B0} under equilibrium. For a degenerate semiconductor with a high doping level and a thin barrier, electron tunneling becomes the dominant conduction mechanism at low temperatures.

The middle panel shows the system under forward bias. The metal is biased positively with respect to the semiconductor, and consequently its Fermi level is lowered with respect to that of the semiconductor in proportion to the applied voltage, V_a. Electrons tunnel predominately from the semiconductor to the metal. The potential barrier seen by these tunneling electrons is lowered from the equilibrium value. Moreover, there is a particular bias voltage, $V_a = V_{min}$, at which the conduction band edge in the semiconductor align with the metal Fermi level. This is the voltage at which a conductance minimum is expected to occur.

Under reverse bias, shown in the right panel, the metal Fermi level is raised above that of the semiconductor and electrons tunnel mostly from the metal into the semiconductor. The potential barrier seen by these electrons however, remains the same as the equilibrium value. This is because the position of the metal Fermi level with respect to the semiconductor conduction band is "pinned" by a high level of density of surface states. Consequently the tunnel barrier height remains the same in spite of the increasing (reverse) applied voltage. The barrier width is thinner than the equilibrium width, however.

Therefore the barrier height seen by tunneling electrons is asymmetric with respect to the bias polarity, and consequently the tunneling conductance is asymmetric. In addition, a conductance minimum is expected to occur at a bias equal to the Fermi degeneracy of the semiconductor. For an n-type semiconductor the minimum occurs at forward bias whereas for a p-type it will happen at a reverse bias. Thus tunneling spectroscopy of a *Schottky-Barrier* tunnel junction can be used to identify dopant type as well as doping level of a semiconductor.

The systematic behavior of our junctions is qualitatively consistent with the scenario for a *Schottky* tunnel junction with a p-type semiconductor. It is not surprising that the surface of a YBCO thin film should behave like a semiconductor. Since YBCO in the normal state is a metal with a low carrier density which is close to the limit of a metal-insulator-transition, any disorder at the surface will render it semiconducting, even insulating.

At a quantitative level, a theory of electron tunneling in *Schottky* junctions has been worked out by Conley and Mahan [7]. Their theory applies to a metal/n-type semiconductor junction. We modified their theory to apply it to the case of a p-type semiconductor. Numerical calcula-

<div align="center">20</div>
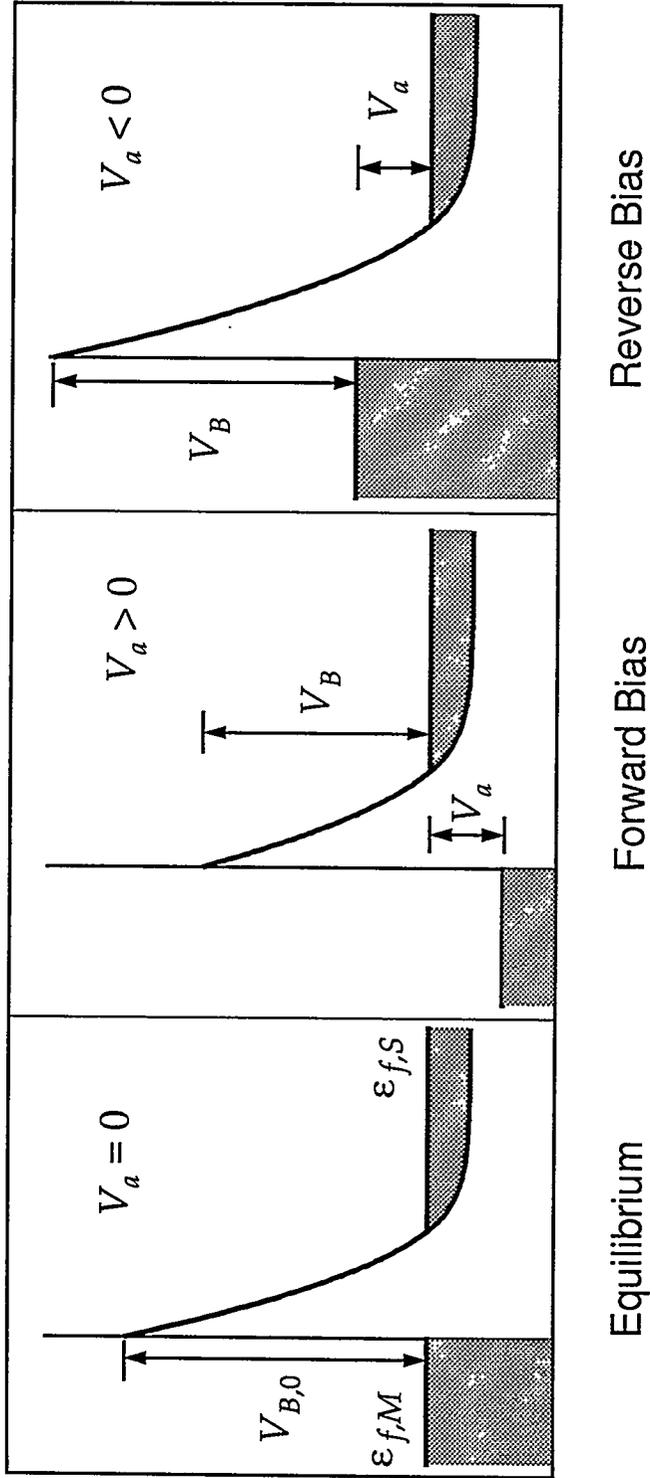
Figure 3: The *Schottky-Barrier* model for a metal/semiconductor junction

G_d/G_d (100 mV), $G_d = dI/dV$

2.4

2.0

1.6

1.2

0.8

0.4

0.0

$V_{B,0} = 0.92$ eV;

$\varepsilon_{f,S} = 0.09$ eV

-200   -100   0   100   200

V (mV)
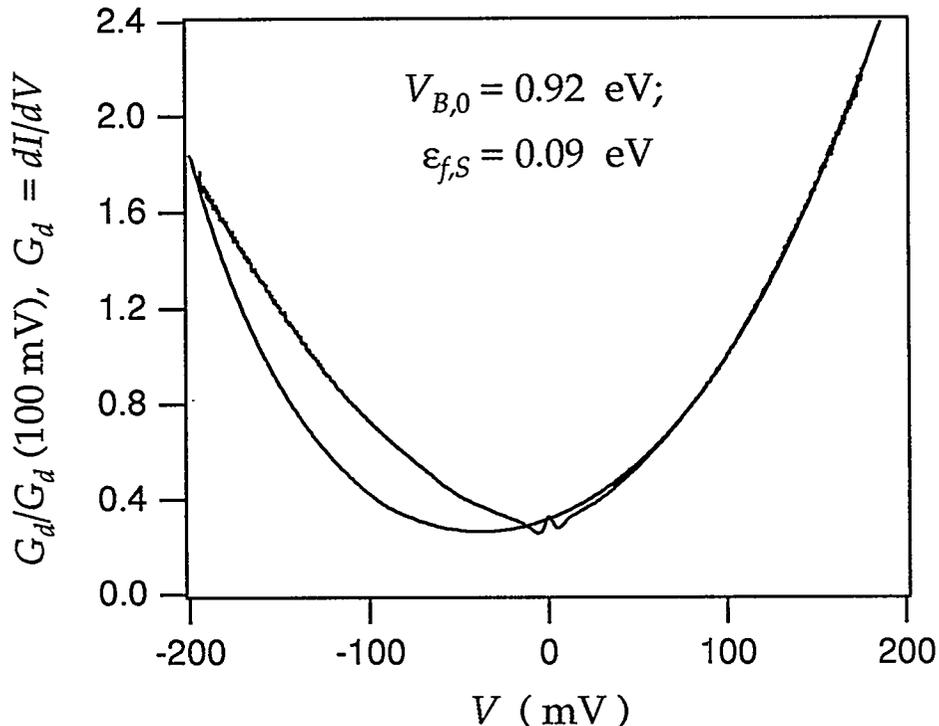
Figure 4: The normalized conductance curve of a tunnel junction (with ZBCP, at 4.2 K) compared with a model calculation (without ZBCP, at 0 K).

tions were carried out for the incremental conductance, dI/dV. The model calculation uses the equilibrium barrier-height, V_{B0}, and the Fermi degeneracy $\varepsilon_{f,S}$ of semiconductor as parameters. Fig. 4 compares the result of a calculation with an experimental curve.

It is important to note that there is a very limited range in which the two parameters can be varied in order for the theory to have an overall agreement with the experiment. This range appeared to be centered at $V_{B0} \simeq 1$ eV for the barrier-height, and at $\varepsilon_{f,S} \simeq 0.1$ eV for the Fermi degeneracy in semiconductor. The parameter values used for the theoretical curve in Fig. 4 are within this range. From the value of the Fermi degeneracy we were able to estimate the carrier density and the carrier effective band-mass for YBCO. They turned out to be 3×10^{21} cm^{-3}, and $m_{eff} \simeq 2.6\,m_0$, where m_0 is the free-electron mass. These values are consistent with known physical properties of YBCO.

Turning now to the quality of the fit between the theory and the experiment, we note that there is quantitative agreement for the forward bias range. For the reverse bias range the theory underestimated the tunneling conductance, although it did produce a broad conductance minimum at about -50 mV. The lack of agreement for the reverse bias range is less serious than it appears, for the model is a simple one and does not take into account the effects of surface disorder and surface states, both of which will enhance the conductance. Disorder, for example, leads to a band-tailing effect that will enhance the conductance predominately at negative bias. To take into account these effects however, will require a degree of knowledge about the YBCO surface which is not currently available. Our study of low-frequency noise of YBCO/Au junction, which will be described next, is our attempt to probe this interface from another perspective.
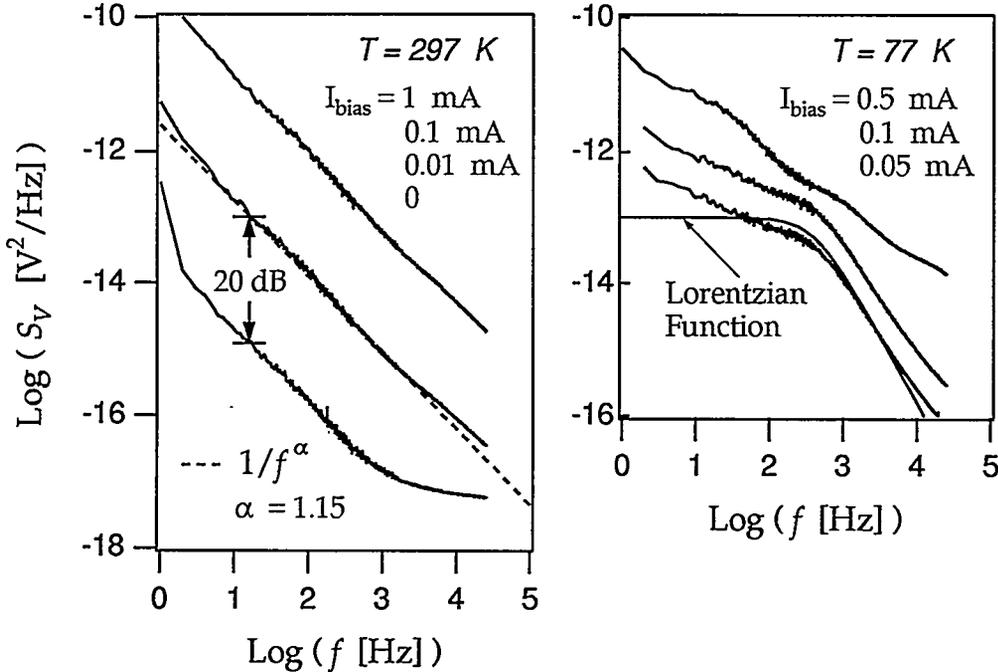
Figure 5: Noise-power-density spectra of a junction for several bias levels.

RESULTS OF LOW-FREQUENCY NOISE STUDY

We see in Fig. 2 that there is considerable conductance noise in our small-area junctions, especially at high bias voltages. The conductance noise has also been observed in many other junctions with areas of 64 μm^2 or larger. Thus these YBCO/Au junctions generally have substantial low-frequency resistance noise. To study junction noise behavior both from a technological and a basic physics point of view, we developed a low-frequency noise measurement system. Technical details of our system have been given in a previous publication [8]. Here we show some important results.

Fig. 5 shows the noise-power-density (NPD) spectra for a junction at room-temperature (left panel) and at 77 K (right panel). The room-temperature voltage noise power density has the usual $1/f$ frequency dependency, with a simple power-law dependence on bias current: $S_V(f) \propto I_b^2$, as indicated by the 20 dB increase in $S_V(f)$ for a ten times increase in bias current. This result allows a simple estimate of the *normalized* resistance fluctuation in a unit bandwidth. At 10 Hz, this figure is $\delta R/R \simeq 6 \times 10^{-4} / \sqrt{Hz}$. Moreover, this figure can be used to estimate resistance noise at any frequencies and for any given bandwidth. It thus offers an enormous practical advantage for engineering high-T_c superconductors electronic devices.

The NPD spectra at 77 K are more complicated. As indicated in the right half of Fig. 5, for small bias they resemble closely a Lorentzian function, which is frequency independent up to a characteristic frequency, beyond which the power-density rolls off as $1/f^2$. A Lorentzian spectrum indicates two-level-fluctuators (TLF), which switch between two quasi-stable levels in an energy space. Rogers and Buhrman [9] showed how small tunnel junction noise behavior can be understood in terms of these TLF's, acting either independently or with interactions between them.

A clearer demonstration of TLF in our junctions is given in Fig. 6, taken at 4.2 K for a
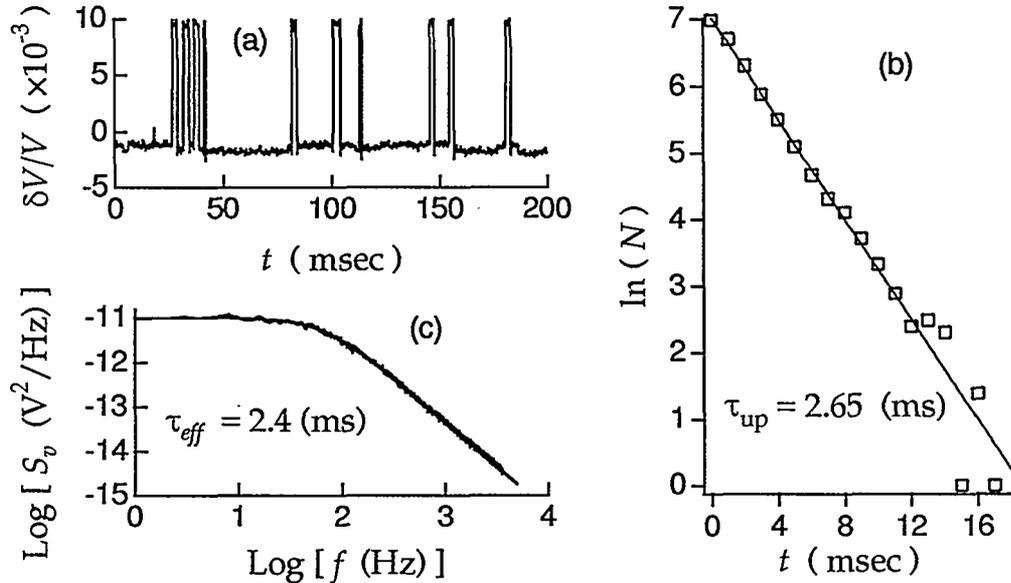
Figure 6: Analysis of time-trace of voltage noise for a 16 μm^2 junction at 4.2 K

16 μm^2 junction. Fig. 6(a) shows a timetrace of the junction voltage signal. It can be seen that the voltage switches randomly between two well defined levels, resembling a random telegraph signal (RTS). The relative size of the switches, $\delta V/V$, is about 10%. After acquiring many timetraces like this, it is possible to analyze, for example, the distribution of times that the voltage remained at a given level, say the "upper-state", before the system makes a switch to the "lower-state". The result is shown in Fig. 6(b), which is a histogram for the life-time of the system in the "upper-state". It obeys a simple exponential dependence, and the inverse of the slope of the exponential decay is the mean-life-time for the upper-state, which for this particular case is 2.65 ms. Applying the same statistical analysis to the "down-state" we found its mean-life-time to be 25 ms.

Machlup [10] showed how the power-density spectrum for a random-telegraph-signal can be calculated, given the mean-life-time of the two levels and the magnitude of the switch. Using his analysis we calculated the power-density spectrum for the voltage noise of our junction, and it fits the experimentally obtained noise spectrum almost perfectly. This is shown in Fig. 6(c).

We note that the effective switch time of the random-telegraph noise of this device is 2.4 ms. Taking the inverse of this, we determine that the characteristic frequency of the Lorentzian spectrum is about 400 Hz. Similar switching behavior, with a characteristic frequency of several hundred hertz, was observed by Myers et al. [11] in YBa$_2$Cu$_3$O$_{7-\delta}$/CaRuO$_3$/YBa$_2$Cu$_3$O$_{7-\delta}$ Josephson junctions. It therefore appears to be a rather general feature of YBCO interfaces.

Rogers and Buhrman [9] identified the origin of two-level fluctuations with electron trapping and release by defect states in the tunnel barrier. In our system the most probable candidates for such defect states are the surface and interface states of YBCO. We have shown indirect evidence for these states from our transport measurements. Our low-frequency noise data provide more direct evidence. Further experiments are needed to probe the energy distribution of these states. This information will in turn enable us to improve on the *Schottky-Barrier* model to better account for the tunneling characteristics of YBCO/Au junctions.

References

[1] Yizi Xu, J. W. Ekin, C. C. Clickner, and R. L. Fiske. Oxygen annealing of YBCO/Gold thin-film contacts. In U. Balu Balachandran et al., editors, *Advances in Cryogenic Engineering Materials*, volume 44, Part B, pages 381–388, New York, 1998. Plenum Press.

[2] Chia-Ren Hu. Midgap surface states as a novel signature for d-wave superconductivity. *Phys. Rev. Lett.*, **72**(10):1526, 1994.

[3] J. W. Ekin et al. Correlation between d-wave paring behavior and magnetic-filed-dependent zero-bias conductance peak. *Phys. Rev. B*, **56**:13746, 1997.

[4] M. Covington et al. Observation of surface-induced broken time reversal symmetry in $YBa_2Cu_3O_7$ tunnel junctions. *Phys. Rev. Lett.*, **79**(2):277, 1997.

[5] M. Fogelström, D. Rainer, and J. A. Sauls. Tunneling into current-carrying surface states of high-T_c superconductors. *Phys. Rev. Lett.*, **79**(2):281, 1997.

[6] J. M. Valles, Jr. et al. Electron tunneling into single crystal of $YBa_2Cu_3O_{7-\delta}$. *Phys. Rev. B*, **44**:11986, 1991.

[7] J. W. Conley and G. D. Mahan. Tunneling spectroscopy in GaAs. *Physical Review*, **161**(3):681, 1967.

[8] Yizi Xu, J. W. Ekin, and C. C. Clickner. Low-frequency noise in YBCO/Au junctions. In *IEEE Trans. Appl. Supercond.*, 1999. Pcoceedings of 1998 Applied Superconductivity Conference, Palm Springs, California, 1998.

[9] C. T. Rogers and R. A. Buhrman. Composition of $1/f$ noise in metal-insulator-metal tunnel junctions. *Phys. Rev. Lett.*, **53**(13):1272, 1984.

[10] Stefan Machlup. Noise in semiconductor: Spectrum of a two-parameter random signal. *J. Appl. Phys.*, **25**:341, 1954.

[11] K. E. Myers, K. Char, M. S. Colclough, and T. H. Geballe. Noise characteristics of $YBa_2Cu_3O_{7-\delta}/CaRuO_3/YBa_2Cu_3O_{7-\delta}$ Josephson junctions. *Appl. Phys. Lett.*, **64**(6):788–790, 1994.

AN EFFICIENT NEAR-FIELD MICROSCOPE FOR THERMAL MEASUREMENTS

G. S. Kino, D. A. Fletcher, K. B. Crozier, K. E. Goodson, and C. F. Quate

Ginzton Laboratory, 450 Via Palou, Stanford University, Stanford CA 94305-4085
Tel: 650-723-0205, Fax: 650-725-2533, EM: kino@stanford.edu

ABSTRACT

We describe the application of the solid immersion lens (SIL) to scanning near-field infrared microscopy. The advantage of the SIL over other near-field approaches is its high efficiency. With the use of micromachined silicon lenses of a few microns diameter, a spot size of 1 μm can be obtained at 5 μm wavelength. The microscope will be used to measure the temperature of interconnects in integrated circuits, which are being excited by high speed pulses and for infrared spectroscopy of small samples such as GaAs laser diodes.

INTRODUCTION

This paper is a progress report on the development of a new technique for infrared measurements of temperature distribution and the emission spectrum with high spatial definition of small scale semiconductor devices with feature sizes as small as 100 nm. Since standard microscopes are so difficult to make in the far infrared range and their definitions are inadequate for modern requirements, we are proposing a different approach, scanning optical microscopy using microscopic sized lenses, called *Solid Immersion Lenses* (SIL), a few microns in diameter mounted on cantilevers. These lenses, made by conventional methods in the millimeter size range, were invented at Stanford by Kino and his coworkers,[1,2,3] and are now being investigated for use in high density optical storage by a number of manufacture such as TeraStor in this country and Sony and Nikon in Japan. It is our intention to use SILs for efficient near-field imaging to obtain focused spot sizes well below the normal diffraction limits of standard microscopy.

We use micromachining techniques to manufacture these microscopic sized lenses. This technology is inexpensive and with it devices can be made and reproduced in large quantities. This method of manufacturing and assembling optical microscope components gets us away from the conventional 19th century approach of lapping and grinding lenses, and then assembling them by hand. At the same time the SIL yields better definitions than were heretofore available and, because of the small lenses employed, the possibility of being able to place the tip of the lens extremely close (100 nm) to the sample being measured, with low chromatic and spherical aberration and relatively uncritical lens design.

PRINCIPLE OF OPERATION OF THE SOLID IMMERSION LENS

It is extremely difficult to make even a standard infrared microscope. The objective lenses are not easily available and must be made of unusual materials such as germanium and silicon, and in the rare instances when they can be obtained are extremely expensive. The spot size, defined as the distance between half power points of the focused beam in an optical microscope, optical storage system or lithography system is determined by diffraction to be approximately $\lambda/(2NA)$, where λ is the

free space wavelength, and *NA* is the numerical aperture of the objective lens defined by the relation $NA = n \sin\theta_0$, where θ_0 is the maximum ray angle to the axis. For an infrared microscope with $\lambda = 5$ μm and $NA = 0.7$, the spot size defined this way is 3.6 μm.

One approach for improving the definition is to employ near-field optics in the manner described by Betzig.[4] In his near-field scanning optical microscope (NSOM), he used a tapered optical fiber covered with a metal film with a small pinhole at the end. The definition of the system is determined by the size of the pinhole rather than by diffraction, and can be 50 nm or less. The advantages of the system are its excellent definition and its polarization preserving capability. A major disadvantage of this approach is its poor light efficiency with 30 to 50 dBs of transmission loss.

An oil or water immersion lens, because the liquid has a higher refractive index than air, may have a numerical aperture greater than one. However liquid immersion is unsuitable for rapid scanning, or for use with semiconductors, a liquid may attenuate in the infrared, and the maximum refractive index available is less than 1.5. Instead, our aim has been to use transparent solid materials in the form of a *Solid Immersion Lens* (SIL), which can have a refractive index of as much as 4.[1,5] This device keeps some of the advantages of a liquid immersion lens and of near-field imaging but with much better efficiency than the NSOM. One form of the SIL, Fig. 1(a), is a hemispherical lens placed between the objective and the sample. Rays enter the SIL along its radii from an objective and converge to its center. If the refractive index of the SIL is n, the wavelength within it is reduced by $1/n$ and consequently the effective numerical aperture $NA_{effective}$ of the objective lens is increased by the refractive index n and the spot size decreased by a factor $1/n$. As an example, for imaging in the infrared at a wavelength of 5 μm, using a silicon SIL with a refractive index of 3.4, and an objective with a numerical aperture of 0.7, the definition would be 1.05 μm. This is a near-field system because the rays at an angle θ such that $\sin\theta > 1/n$ are totally internally reflected at the solid-air interface, and the fields corresponding to these rays fall off exponentially in air. Consequently the object to be observed must be placed close to the SIL.

A second type of SIL, illustrated in Fig. 1(b), the supersphere, is based on the idea that a beam can be focused perfectly to a point inside a sphere a distance a/n from its center. In this case, a ray entering at an angle θ_I to the axis would be refracted to an angle θ_T from the axis, where $\sin\theta_T = n \sin\theta_I$, and the effective *NA* is increased by a factor n^2. So it is possible to work with an objective with a relatively small numerical aperture. There is a limit on the maximum effective numerical aperture obtainable because the input beam must be incident on the SIL surface above the focal point on the sphere where the angle to the axis of the refracted ray is $\theta_T < \pi/2$. Thus, the maximum angle of incidence θ_i is given by the relation $\sin\theta_i = 1/n$ and the maximum effective numerical aperture that can be obtained is still $NA_{effective} = n$. For the example given above, we would only need an objective with a numerical aperture of 0.2.

In our first experiments with solid immersion microscopy, we used a confocal microscope with a long working distance objective of numerical aperture 0.8 with an illumination wavelength of 436 nm, and a hemispherical solid immersion lens with a refractive index of 1.9 placed under it.[1,5]
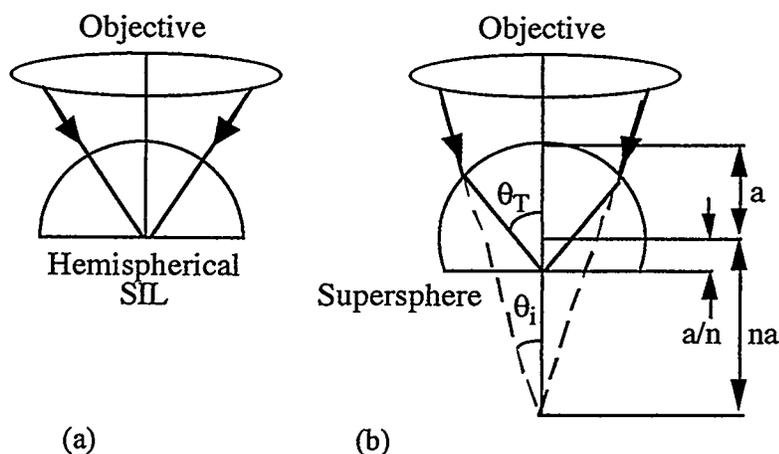
Fig. 1. Solid immersion lens. (a) hemispherical lens. (b) aplanatic focusing SIL or supersphere.

The SIL had a $NA_{effective}$ of 1.52 and was used to image various small structures at a wavelength of 436 nm. The smallest structures imaged were the 100 nm lines and spaces in photoresist shown in Fig. 2. In comparison, the smallest structures that were observed with the confocal microscope, with a 0.9 N.A. objective under the same conditions were 150 nm lines and spaces with a calculated minimum detectable periodicity of 242 nm (120 nm lines). The calculated minimum detectable periodicity for the SIL is 144 nm (72 nm lines).
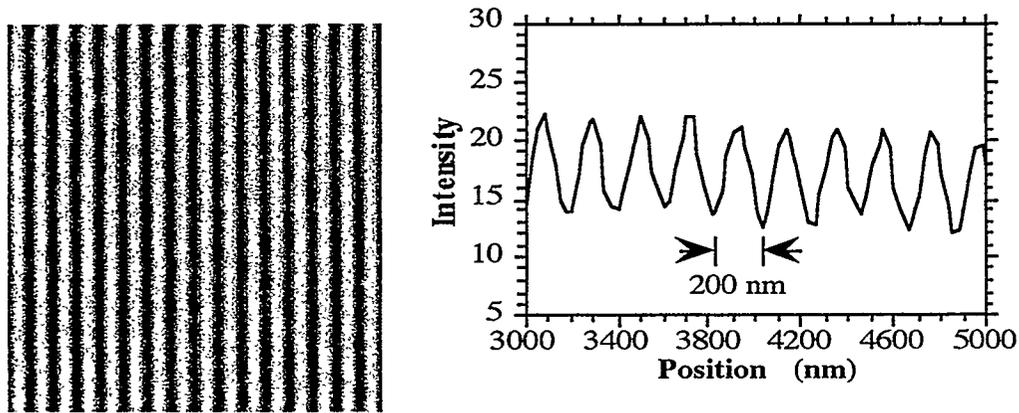
Fig. 2. Image and line scan of a 200 nm period grating.

Air gap (μm)	Spot size (μm)	Maximum Intensity	Relative power
0	0.98	1	1
0.1	1.04	0.70	0.84
0.2	1.09	0.48	0.68
0.3	1.12	0.34	0.55
0.4	1.19	0.18	0.35
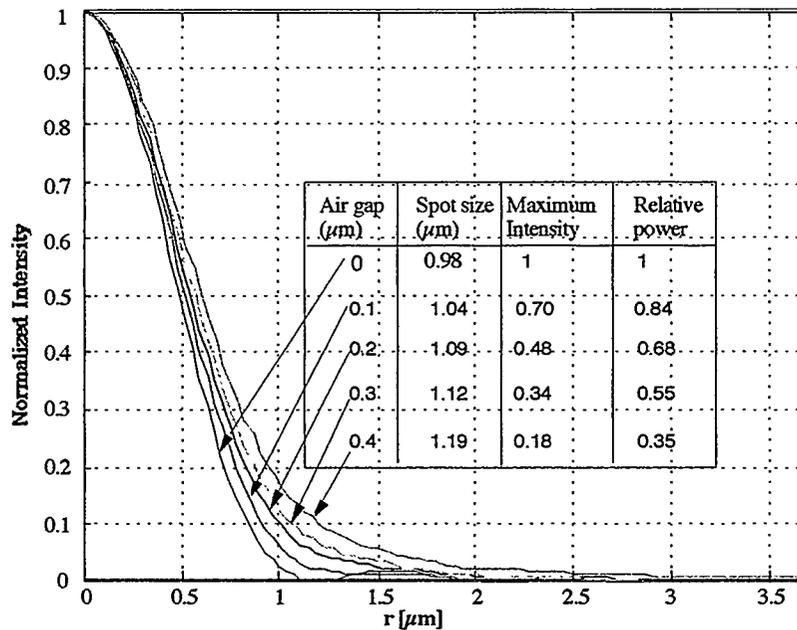
Fig. 3. Point spread functions for normalized intensity with different air gaps.

One question that arises with the use of an SIL is the effect of an air gap between the SIL and the image plane on the point spread function (PSF) and the transmission efficiency. Codes based on vector field theories have been developed for determining the fields outside the lens in air and in multiple layer systems such as that of an optical disk or photoresist on silicon[6,6] The conclusion of these computations is that in the optical range, with SILs with a refractive index of 2 or so, the transverse resolution between half power points, d, is given fairly accurately by the simple formula $d = \lambda/2NA_{eff}$ where $NA_{eff} = n \sin \theta_0$ n is the refractive index of the SIL and θ_0 is the maximum ray angle from the axis within the lens, provided that the air gap is kept to less than 100 nm at a wave length of 0.7 μm. For higher refractive index materials or shorter wavelengths, the air gap must be still thinner. Calculations for the point spread function (PSF) at a silicon substrate for a silicon SIL

with a refractive index of 3.4, working at a wavelength of 5 μm are shown in Fig. 3. It will be seen that the spot size between the half power points is 0.98 μm with no air gap. But as the air gap is increased the spot size increases by 10% with an air gap of 0.2 μm and the intensity on axis drops to 48% and total power to 68% at this point. If the SIL were used as a receiver of thermal radiation, the efficiency would again be 68% with an air gap of 0.2 μm. This efficiency is far higher than that of the NSOM.

We are also concerned with the tolerance for manufacturing these lenses. An image formed by the input beam may be shown to be demagnified in the hemispherical SIL by a factor $1/n$ in both the radial and axial directions. The hemispherical SIL is extremely tolerant. By examining when the aberrations due to field curvature become large enough to cause a phase error of $\pi/2$ between the outer and inner rays of a focused beam, we find that the field of view of the hemispherical SIL, Δd_{max} is given by the relation[2,5]

$$\Delta d_{max} = \sqrt{\frac{2a\lambda}{n(n-1)\sin^2\theta_0}},$$ (1)

where a is the radius of the hemisphere. For $\lambda = 436$ nm, $n = 2$, $\sin\theta_0 = 0.8$, $a = 1$ mm, we find that $\Delta d_{max} = 39$ μm. This is a relatively large field of view, and is the reason why the image in Fig. 2 extends over a relatively large region without appearing to be aberrated.

The tolerance in the axial direction is also broad. If the thickness of the hemisphere is changed, the input beam may be refocused to focus on the flat surface provided that the lens thickness varies by less than Δz_{max}, where

$$\Delta z_{max} = \sqrt{\frac{2a\lambda}{n(n-1)\sin^4\theta_0}}.$$ (2)

For a supersphere, it can be shown that to first order in r, the radial demagnification is $1/n^2$ and the field of view is comparable to that of the hemispherical lens. The demagnification in the z direction is $1/n^3$ However there is a first order error in the length tolerance, Δz_{max} which can be shown to be given by the approximate formula:

$$\Delta z_{max} \approx \frac{n}{n^2-1} \frac{\lambda}{2\sin^2\theta_0},$$ (3)

where θ_0 is the maximum ray angle inside the lens. Using the same parameters as for the hemispherical SIL, we find that is 0.3 μm. Thus, the tolerance on the length of a supersphere, of typically 1 to 3 mm diameter, is very tight although, for $n = 2$, the tolerance on the axial position of the objective is eight time (n^3) this value. However for silicon, at a wavelength $\lambda = 5$ μm, with $n = 3.4$, and $\sin\theta_0 = 0.8$, this simple formula gives a tolerance in the position of the objective of 49 μm and a length tolerance of 1.25 μm. The reason for the large tolerance is that with a high refractive index, incident rays from air are bent towards the focus and their initial direction becomes relatively uncritical.

SCANNING TECHNIQUES

Although it is possible to obtain a large field of view with an SIL, this is not easy to do in practice because it is difficult to keep the flat surface of the SIL close enough over a large area to the object being observe. In our early experiments, we ground off the hemisphere to a conical shape so that the bottom surface would be of the order of 100 μm in diameter. In optical storage the SIL is incorporated into a floating head so that it floats on an air bearing over a rotating disk. But to observe substrates which are not flat, these stratagems are not good enough.

Recently Ghislain and Elings[7,8] have built a different type of near-field microscope using a solid immersion lens. The SIL, as shown in Fig. 4, was tapered at its lower end to a cone half angle of 65°, and a supersphere was used with a material of refractive index 2.2 at a wavelength of 442 nm, and an apodized beam with an $NA_{effective}$ of 2, yielding a theoretical spot size of 120 nm. The SIL was

mounted on a soft cantilever in a force microscope structure (Fig. 5) so that its distance from the sample could be controlled. The tip of the SIL was less than 1 µm diameter, which made it possible to obtain very small spacing between the tip and the sample. The sample was scanned to form a complete image in the same way as with a near-field scanning optical microscope (NSOM). Images were taken of metal films laid down on glass with periodically spaced holes in them. Optical contrast was obtained with a definition of the order of 150 nm. Other features with a definition of the order of 70 nm were observed. This phenomenon was thought to be due to topography effects associated with the exponential fall off of fields away from the tip. Cooperating with us at Stanford, they also carried out photolithography with this same system and obtained good results.[8]

It is our intention to make SILs only a few microns diameter and use micromachining techniques to manufacture them. This eliminates the need for a long working distance objective. The SILs will be mounted on small cantilevers with a rapid response time in the same manner as with scanning force microscopy. In that case the supersphere and even aspherical lenses would become more useful, for now the tolerance of the objective lens position and focusing would be very large. Furthermore, with such small lenses the shape of the lens becomes much less critical, for now errors in phase do not accumulate over a long distance, and so aberrations are far smaller. In addition, by changing the chemical etching conditions there is the possibility of making aspheres so that the input beam could be rectilinear, i.e., we would not need a high power objective lens. We have calculated in some detail the nature of such aspherical lenses which, typically, are elliptical in shape.
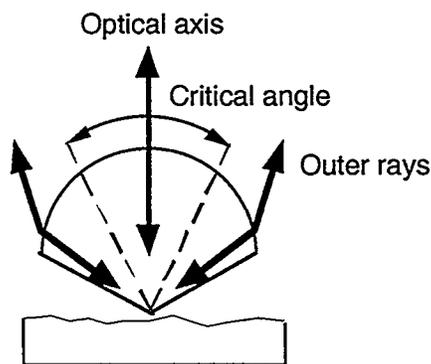
Fig. 4. SIL microscope structure.[7,8]
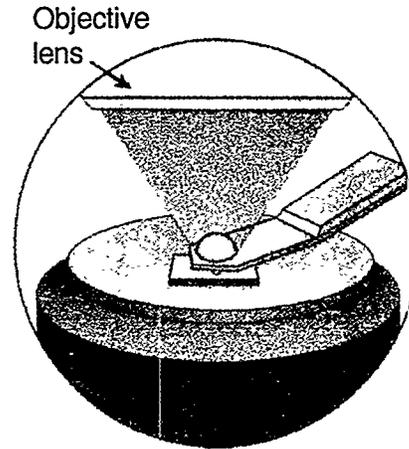
Fig. 5. SIL mounted on a cantilever.[7,8]

As an example of the advantages of using microlenses for eliminating aberrations, we have calculated with the optical design program ZEMAX the point spread function (PSF) of an imperfect hemispherical lens. We took the lens to be a hemisphere of radius a minus a parabola, $r = 0.04z^2$. . The calculated PSFs for two values of the hemisphere radius a, 3.5 µm, and 3.5 µm, with $\lambda = 325$ nm and $n = 2$, are shown in Fig. 6. It will be seen that the PSF of the smallest lens has very low sidelobes, but as the radius of the hemisphere is increased, the sidelobes get worse. With the largest lens, the effect of the nonsphericity is to ruin the PSF. Furthermore, we observe that even though the lens is nonspherical, aberrations are negligible. We conclude that the requirement for a perfect spherical shape becomes less critical as the lens size is reduced to the microscopic dimensions proposed here.

In previous applications, SILs have been shaped with traditional lens-making techniques that are time consuming, labor intensive, and expensive.[7,8] Microfabrication would enable hundreds of SILs as small as 5 µm to be fabricated using standard lithographic tools; the smallest SILs manufactured with mechanical grinding techniques are about 1 mm diameter. An SIL fabricated on the end of an AFM could be scanned above the surface of a sample held within its near field, concentrating light on or collecting light from the sample. Such a device could be used for collecting near-infrared wavelengths transmitted through a cell or thermal radiation from a self-heated interconnect. A major advantage of the use of this type of technology is that the micromachined tip the SIL will also be used as a

Scanning Force Microscope (SFM). This makes it possible to adjust the tip-sample spacing and to make independent measurements of the sample profile.
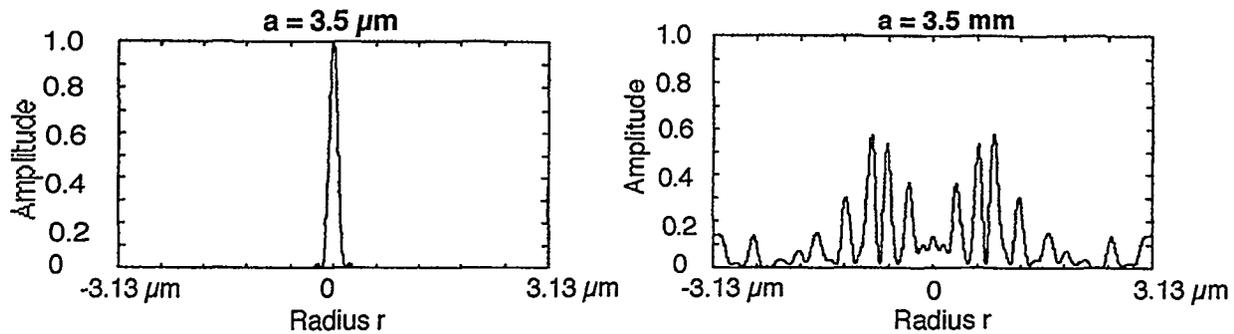
Fig. 6. The PSFs for two different sizes of nonspherical lenses.

FABRICATION OF AN INTEGRATED CANTILEVER AND MICROLENS

Our objective is to demonstrate the optical resolution of an integrated SIL and SFM at infrared wavelengths. Single crystal silicon has been chosen as the lens and cantilever material due to the availability of Si processing techniques and equipment, the proven use of Si cantilevers in scanning probe systems, and the high index of Si at the infrared wavelengths important to spectroscopy, thermometry, and other applications. Scaled down versions of the device illustrated in Figs. 3 and 4 are being fabricated with microlens diameters ranging from 5 to 15 μm and cantilevers from 50 to 200 μm long. In order to localize the region of contact between the sample and the SIL, a tip is formed on the opposite side of the lens. A conical tip with radius of curvature less than 1 μm and sides angled at 60 degrees from the vertical provides sufficient localization without blocking high-angle rays. Such a tip is much larger than the typical NSOM tip and allows easy alignment of the focal point, but it is small enough to allow a very close approach to a rough surface. Because of its relatively large size, it is also not subject to the same wear as an NSOM tip, as has been shown experimentally by Ghislain et al.[7,8] Though many techniques for fabricating sharp, high aspect-ratio tips exist, methods for less-sharp, low aspect-ratio tips with large side angles must be developed.

Fabrication of the integrated SIL cantilever presents two primary processing challenges: (1) formation of the lens shape and (2) double-side processing of a thin film to create a tip opposite the lens. Arrays of microfabricated lenses are used with focal plane array detectors and wave-front sensors, among other devices. The method chosen for use in this work is based on reflow of photoresist pillars and transfer of the shape into a substrate by dry etching[9]. This approach uses standard photolithography to define the diameter of the lens but requires a non-standard dry etch to consume the lens material and photoresist mask at the same rate. A fabrication process (Fig. 7) has been designed to create a microlens and tip on opposite sides of a thin Si cantilever. Pillars are formed in photoresist and reflowed thermally or in acetone vapor to form a three-dimensional etch mask for the lens. The SIL is formed by reactive ion etching (REI) the top Si of a Simox SOI wafer that has had an additional 15 μm of Si grown epitaxially. The selectivity (Si : photoresist) of the etch process and the reflow conditions are used to control the shape of the lens. A thin film of thermal oxide is grown to form an etch stop for the cantilever release. The SOI with SILs is then anodically bonded to a Pyrex wafer with pits etched to protect the lens. The bottom Si and middle oxide of the SOI wafer is removed in TMAH and HF, respectively, leaving the thin top Si layer in which the lens tip and cantilever will be formed. Tips are then formed using reflowed photoresist and RIE opposite the lens. Next, cantilevers are masked and etched into the remaining top Si with RIE, stopping on the thermal oxide previously grown on the lenses. Finally, the thermal oxide is removed with HF and the cantilevers held by the support wafer are released by backside etching or wafer sawing. Note that this process could be used to create lenses and cantilevers in other materials.

31

1. Definepillars in photoresist om an SOI wafer

2. Reflow the photoresist thermally or in acetone vapor to form a curved shape

3. Transfer the curved shape onto Si with RIE

4. Grow thermal oxide on lens surface to serve as an etch stop for backside processing

5. Pattern protective pits in a Pyrex wafer with photoresist

6. Etch the pits with BOE

7. Anodically bond the glass wafer to the SOI wafer

8. Remove the thermal oxide, bulk Si, and buried oxide to expose the back side of the lens

9. Define the lens tip in photoresist

10. Etch the tip with RIE

11. Define the canilever in photoresist

12.. Etch the cantilever with RIE using thermal oxide as an etch stop

photoresist   oxide
silicon   Pyrex

13. Remove the thermal oxide from the cantilever and lens with an HF dip and release the the die with a wafer saw

Fig. 7. Steps in the micromachining of the SIL and tip mounted on a cantilever.

The lens fabrication and cantilever fabrication processes will be joined to make an integrated cantilever and SIL. A critical step in the process is alignment of the tip and distance from the lens to the tip apex. A high-resolution mask aligner will be used for alignment, and thin-film thickness measurements during etching will control thickness.

We expect to be testing our first infrared SILs mounted on cantilevers within the next few months and then to go on to test them first for imaging simple structures and later for measurement of pulsed thermal sources such as interconnects in high speed circuits.

Hemispherical SILs and short focal-length microlenses have been fabricated in single crystal Si. A photoresist reflow method using acetone vapor has been developed, and a plasma etch recipe has been refined to transfer and extrude the photoresist lens shape into Si (Fig. 8). Si cantilevers bonded to Pyrex have been released (Fig. 9). A process for fabricating the Si cantilevers which enables lithography on both sides of the top Si of an SOI has been created.

32
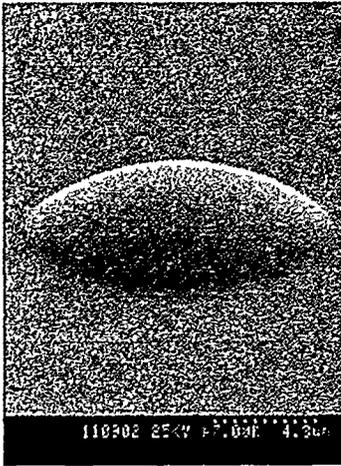
Fig. 8. Microlens in Si.
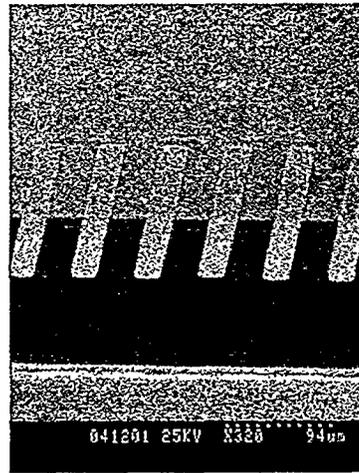
Fig. 9. Released Si cantilevers bonded to Pyrex.

ACKNOWLEDGMENTS

FOOTNOTES

1. S. M. Mansfield and G. S. Kino, "Solid Immersion Microscope," Appl. Phys. Lett. 57, 2615-2616 (1990).

2. S. M. Mansfield, W. R. Studenmund, G. S. Kino, and K. Osato, "High Numerical Aperture Lens System for Optical Storage," Opt. Lett. 18, 305-307 (1993).

3 . I. Ichimura, S. Hayashi, and G. S. Kino, "High Density Optical Recording Using a Solid Immersion Lens," Appl. Opt., 36, 4339-4348, (1997).

4. E. Betzig, J. K. Trautman, R. Wolfe, E. M. Gyorgy, P. L. Finn, M. H. Kryder and C. H. Chang, "Near-Field Magneto-Optics and High Density Data Storage," Appl. Phys. Lett. 61, 142 (1992).

5. S. M. Mansfield, "Solid Immersion Microscopy," Ph.D. Dissertation, Department of Applied Physics, Ginzton Laboratory, Stanford University (March 1992).

6. M. Mansuripur, "Effects of High-Numerical-Aperture Focusing on the State of Polarization in Optical and Magneto-Optic Data Storage Systems," Appl. Opt. 30, 3154-3162, (1991).

7. L. P. Ghislain and V. B. Elings, "Near-Field Scanning Solid Immersion Microscope," Appl. Phys. Lett. 72, 2779-81 (1998).

8. L. P. Ghislain, V. B. Elings, K. B. Crozier, S. R. Manalis, S. C. Minne, K. Wilder, G. S. Kino, and C. F. Quate "Near-Field Photolithography With a Solid Immersion Lens," Appl. Phys. Lett. 74 501 (1999).

9. T. Serikawa and S. Shirai, "Modelling of Lift-Off Sputter Deposition and Application to Fabrication of a Microlens," Thin Solid Films, 281-282, 246-248 (1996).

33

ELECTROMECHANICAL FRACTURE IN PIEZOELECTRIC CERAMICS

Huajian Gao and David M. Barnett

Division of Mechanics and Computation
Stanford University
Stanford, CA 94305, U.S.A.

ABSTRACT

The reliable operation of smart devices and structures depends on the integrity of the materials chosen for sensor and actuator components. We investigate the cracking behavior of piezoelectric ceramics, brittle materials whose nonlinear response is dominated by electrical effects. We simulate these microstructural effects using discrete electric dipoles, and find that the crack driving force at the local length scale is expressed solely in terms of mechanical opening stresses. The resulting predictions of failure under combined electromechanical loading conditions agree qualitatively with empirical observations. An investigation of permeable surface conditions reveals that the effect of air inside an open crack is negligible except in the case of an almost perfectly sharp crack.

INTRODUCTION

The growing demand for smart systems and structures raises concerns about the mechanical integrity of the materials used for sensor and actuator components. In this study we attempt to resolve some basic discrepancies between theoretical predictions and empirical observations of the cracking behavior of piezoelectric ceramics, some of the most widely used transducer materials. Numerous experimental studies have been performed on specimens of lead zirconate titanate (PZT) with cracks perpendicular to the poling axis, loaded by tension and electric field along the axis. In compact tension, three-point bending, and Vickers indentation tests, researchers have found that the application of electric field aligned with the material poling direction promotes cracking, while the opposite sense of the field inhibits cracking [1, 2]. However, the natural extension of linear elastic fracture mechanics to account for electrical contributions to the energy balance predicts that the field should inhibit fracture irrespective of its sign [3, 4, 5].

Some attempts have been made to explain the empirical results in terms of the permeability of the crack interior and the resulting change in boundary conditions once the crack opens [6, 7, 8]. But we show that the inhomogeneous crack-face conditions cannot alter the essential character of the relationship between applied field and critical stress. Further, if the medium that fills the crack is air, it plays a negligible role except in the case of extremely slender initial voids. A more

promising possibility for resolving the fundamental discrepancy involves a consideration of non-linear material effects, specifically in the ceramic's electrical behavior. By adopting a multiscale framework, we isolate the electrical nonlinearity, and introduce a physics-based description of the domain saturation and switching that control the electrical response at the local level. We model these effects using discrete electric dipoles superimposed on a medium with homogeneous linear properties, and develop a fracture criterion based on the local stress intensities. The resulting predictions for the dependence of failure load on applied field agree qualitatively with the experimental results mentioned above

In this paper we present an outline of the solution method and the essential results; more details can be found in Fulton and Gao [9].

LINEAR THEORY

The constitutive behavior of a general linear piezoelectric material is described by the pair of coupled equations

$$\sigma_{ij} = C_{ijkl}\, s_{kl} - e_{lij}E_l \tag{1}$$

$$D_i = e_{ikl}\, s_{kl} + \varepsilon_{il}E_l\,, \tag{2}$$

where

$$s_{kl} = \frac{1}{2}\left(u_{k,l} + u_{l,k}\right) \tag{3}$$

is the strain tensor corresponding to the displacement vector u;

$$E_l = -\phi_{,l} \tag{4}$$

is the electric field vector in terms of the potential ϕ; σ is the stress tensor; and D is the electric displacement vector. The material constants are given by the stiffness tensor C, the piezoelectric coefficients e, and the dielectric permittivity values ε (measured at constant strain). Subsequent formulas can be simplified considerably if we introduce the shorthand notation

$$\tau_{iJ} = \begin{cases} \sigma_{ij} & \text{if } J = 1,2,3 \\ D_i & \text{if } J = 4, \end{cases} \tag{5}$$

along with the convention that lower-case Latin subscripts range from 1 to 3, upper-case subscripts range from 1 to 4, and repeated Latin indices signal a sum over the appropriate range. Then, in the absence of body forces and free charges, the equilibrium equations are expressed succinctly as

$$\tau_{iJ,i} = 0\,. \tag{6}$$

Planar solutions can be obtained using the techniques developed by Stroh [10] for anisotropic elasticity and extended by Barnett and Lothe [11] to account for piezoelectric coupling. We adopt their formulation of the resulting eight-dimensional eigenvalue problem, as well as their scheme for ordering the eigenvalues p_α and scaling the eigenvectors $\{A_\alpha, L_\alpha\}$. We then define the 4×4 real matrices

$$B_{JK} = \frac{1}{4\pi}i\sum_{\alpha=1}^{8} \pm L_{J\alpha}L_{K\alpha} \tag{7}$$

$$T_{JK} = i\sum_{\alpha=1}^{8} \pm p_\alpha A_{J\alpha}L_{K\alpha}\,. \tag{8}$$

35

The problem of an insulated crack in a linear piezoelectric has been studied extensively [3, 5, 12], and its solution is well known. For a crack in the (x_1, x_2)-plane, bounded by $|x_1| < a$, the boundary conditions can be written succinctly as

$$\tau_{2I}(x_1, 0) = 0, \quad |x_1| < a. \tag{9}$$

The four intensity factors are derived from

$$K_J = \lim_{x \to 0} \sqrt{2\pi |x|}\, \tau_{2J}(x), \tag{10}$$

in terms of the remote loading τ_{ij}^∞. The energy release rate then takes the compact form

$$G_{\text{linear}} = \frac{1}{8\pi} K_J B_{JL}^{-1} K_L \tag{11}$$

$$= \frac{a}{8} \tau_{2I}^\infty B_{IJ}^{-1} \tau_{2J}^\infty. \tag{12}$$

These formulas apply to cracks at arbitrary orientations in general linear piezoelectric materials under any combination of remote loads. However, they cannot explain experimental observations, even for the relatively simple case of a crack perpendicular to the poling of a transversely isotropic sample, subjected to Mode I stress and electric field along the poling axis. As mentioned at the outset, estimates of the failure load obtained from (11) or (12) show an even functional dependence on applied field, while empirical data suggest an odd dependence. The remainder of the paper is devoted to finding a resolution to this contradiction.

PERMEABLE BOUNDARY CONDITION

The analysis of the previous section depends on the idealized approximation that the crack surfaces remain perfectly insulated during loading. However, in many experiments and in almost all practical applications, upon opening the crack interior fills with an electrically permeable fluid, usually air. It has been suggested [7, 8] that the resulting inhomogeneous boundary condition plays a significant role in the fracture of piezoceramics. We now examine the effects of treating the fluid inside the crack realistically, as an isotropic dielectric with no stiffness.

When a slit crack opens into an elliptical profile, the deformed medium can be treated as a bimaterial inclusion problem. For elastic bodies subjected to uniform far-field stresses, Eshelby [13] showed that the strain inside an ellipsoidal inclusion is a constant. Deeg [14] generalized the method to apply it to piezoelectric materials, where the applied fields include electric displacements as well as tractions. He showed that the fields induced in an ellipsoidal piezoelectric inhomogeneity, both strains and electric field, are constant under any uniform remote loading conditions. As a particular case of Deeg's result, we can take the inclusion to be a dielectric material, with no stiffness or piezoelectric coupling. In short, we conclude that, when uniform electromechanical loads are applied to a cracked piezoelectric solid, the fluid that fills the crack has a constant electric field $\bar{E}$.

Now, in the absence of free charge on the crack surfaces, the electric displacement normal to the interface must be continuous. Within the constraints of infinitesimal deformation theory, the flux on the solid side of the interface can be approximated by τ_{24} over virtually the entire crack length. Meanwhile, the flux in the fluid is equal to the constant value $\bar{\varepsilon}\bar{E}_2$, where $\bar{\varepsilon}$ is the permittivity of the medium that fills the crack. The continuity of the electric displacement, together with the traction-free conditions on the crack surfaces, can be expressed as

$$\tau_{2I}(x_1, 0) = \delta_{I4}\bar{\varepsilon}\bar{E}_2, \quad |x_1| < a. \tag{13}$$

But we can also relate the electric field within the crack to the voltage difference across the fluid and the crack-opening displacement:

$$\Delta\phi(x_1) = -\bar{E}_2 \Delta u_2(x_1). \tag{14}$$

These conditions are sufficient to solve for the fields throughout the bimaterial.

Because the fluid stores electrostatic energy, an overall energy balance must be performed to determine the portion of the work done on the specimen boundary available to drive the crack. The work that is stored in the solid is given by the piezoelectric enthalpy $\mathcal{W}^{\text{sol}}$, and that stored in the fluid is the electrostatic energy $\mathcal{U}^{\text{fl}}$. With the presumption of fixed grips ($d\Delta = 0$) and fixed voltage ($dV = 0$) at the boundary, the crack driving force consists of contributions from both media:

$$G = G^{\text{sol}} + G^{\text{fl}}, \tag{15}$$

where

$$G^{\text{sol}} = -\left(\frac{\partial \mathcal{W}^{\text{sol}}}{\partial A}\right)_{\Delta,V}, \qquad G^{\text{fl}} = -\left(\frac{\partial \mathcal{U}^{\text{fl}}}{\partial A}\right)_{\Delta,V}, \tag{16}$$

and dA is an increment of crack area.

Using the definition (10), we find the intensity factors for the permeable crack,

$$K_J = \left(\tau_{2J}^{\infty} - \delta_{J4}\bar{\varepsilon}\bar{E}_2\right)\sqrt{\pi a}, \tag{17}$$

and we can express the solid's contribution to the energy release rate as

$$G^{\text{sol}} = \frac{1}{8\pi} K_J B_{JL}^{-1} K_L. \tag{18}$$

Substituting expressions for the crack-opening displacements into (14) yields

$$\bar{E}_2 = \frac{1}{2\bar{\varepsilon}B_{24}^{-1}}\left[\left(B_{2J}^{-1}\tau_{2J}^{\infty} - \bar{\varepsilon}B_{44}^{-1}\right) - \sqrt{\left(B_{2J}^{-1}\tau_{2J}^{\infty} - \bar{\varepsilon}B_{44}^{-1}\right)^2 + 4\bar{\varepsilon}B_{24}^{-1}B_{4J}^{-1}\tau_{2J}^{\infty}}\right]. \tag{19}$$

The method can be applied to arbitrary loading situations, but in many problems of interest there is enough symmetry so that $\bar{E}_1 = 0$. In this case the fluid's contribution to the crack driving force takes the form

$$G^{\text{fl}} = -\frac{a}{8}\bar{\varepsilon}\bar{E}_2^2 B_{2J}^{-1}\left(\tau_{2J}^{\infty} - \delta_{J4}\bar{\varepsilon}\bar{E}_2\right), \tag{20}$$

and the total energy is given by (15), (18), and (20).

ELECTRICAL NONLINEARITY

The class of piezoceramic materials we are interested in typically displays extremely brittle mechanical response with almost no plasticity. The electrical behavior, on the other hand, exhibits significant nonlinear characteristics, most notably the hysteresis associated with polarization switching. In fact, it can be shown that the region of electrical nonlinearity around a crack tip in a piezoceramic dwarfs the mechanical nonlinear zone. It is reasonable, therefore, to separate the length scales at which electrical and mechanical nonlinear effects play a role. In this section we
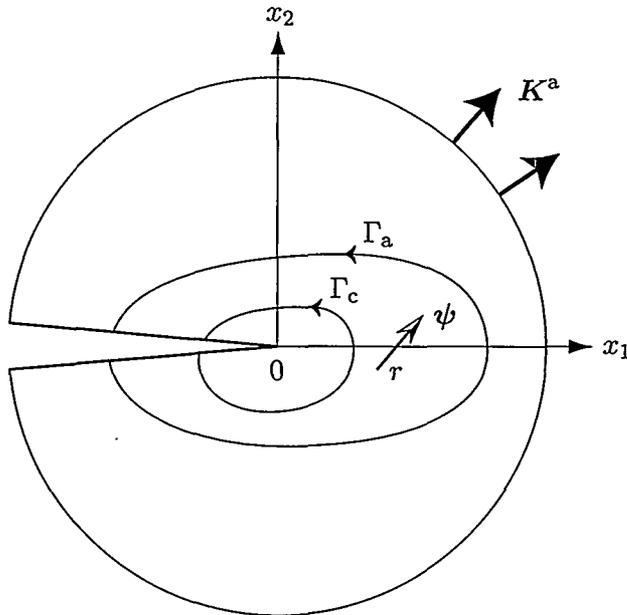
Figure 1: Crack Interacting with a Discrete Dipole.

focus on an intermediate length scale, at which the stress fields appear to follow linear constitutive laws, while the electric field exhibits nonlinearity. In this framework, we develop a model for electrical nonlinearity based on the switching behavior of polar domains in ferroelectrics.

When a uniform low-level electric field is applied to a piezoelectric solid, the internal polarization appears to respond in a linear homogeneous fashion. But this macroscopic behavior is the aggregate effect of a vast collection of randomly oriented ferroelectric domains. Upon closer inspection, these local inhomogeneities gain significance and, as the electric field is intensified, may dominate the material response. We simulate the local complexity directly, using discrete electric dipoles superimposed on a homogeneous medium with the macroscopic piezoelectric properties. Each dipole represents the deviation of a given domain's polarization vector from the response predicted by the linear constitutive law. Now, while a dipole ψ in a uniform electric field is at equilibrium, any variation in the field results in a net force:

$$F = (\nabla E)\,\psi. \tag{21}$$

Because the region surrounding a crack tip is characterized by severe gradients in all the field quantities, the crack exerts a net force on dipoles representing the nearby polar domains. This non-local interaction implies that an energy density formulation cannot capture the type of nonlinear material effects we are investigating; they can only be understood within the multiscale framework.

As a first approximation to the case of general nonlinearity around a crack tip, we examine the effect of a single dipole in the plane of the crack, as shown in Fig. 1. It is meant as a simplified characterization of the net effect of the many dipoles needed to describe any deviations from linear behavior. The influence of the dipole must then be sufficient to cancel the crack-tip singularity in the electric displacement; this condition fixes the dipole strength for a given position r. If a J-integral were calculated for the contour labeled Γ_a, the result would be the linear estimate of the crack driving force, given by (11). But the dipole represents the material microstructure, so the contour Γ_c must be used to capture the local driving force; the resulting J-integral corresponds to

38

a crack cleaving the microstructure. The difference between the "apparent" and local J-integrals is precisely the force exerted on the dipole by the crack.

For an insulated crack, the local energy release rate can be expressed in terms of the local intensity factors K^c as

$$G_c = \frac{1}{8\pi} K_J^c B_{JL}^{-1} K_L^c. \tag{22}$$

If the cracked sample is transversely isotropic, and the loading is symmetric, the relationship between local and apparent intensity factors is captured by

$$K_J^c = K_J^a - \frac{T_{4J}}{T_{44}} K_4^a, \tag{23}$$

where $K_J^a = \tau_{2J}^\infty \sqrt{\pi a}$. From the form of the energy release rate (22) it is immediately apparent that the onset of fracture is determined solely by the local intensity factors K_J^c. The fact that the electrical intensity K_4^c vanishes indicates that, at the local length scale, the crack extension is driven by purely mechanical opening forces. In other words, the combination of electrical and mechanical loads applied in the global view are experienced as "effective" mechanical intensities at the local level. These effective stresses can be interpreted in terms of the mismatch strains associated with local domain switching.

In the case of a fluid-filled crack, the solid's contribution to the driving force is evaluated at the local level, and is given by (22) and (23), with the apparent intensity factors for a permeable crack (17). The contribution from the fluid, however, is dominated by the overall expansion of the elliptical cavity, so its treatment is accomplished completely at the global level. The effect can be calculated from (19) and (20).

The analysis of these problem reveals a remarkable feature: the local energy release rate is in fact independent of both the dipole's position r and its strength ψ. This invariance is particularly valuable because it allows us to sidestep the difficulties normally associated with characterizing the local electrical response of ferroelectrics. That is, although an understanding of the microstructure is vital to the development of our local model, the end results are independent of the specific material details. What makes the theory powerful is that it takes account of the complicated nature of electrical nonlinearity without requiring any extra experimental measurements.

NUMERICAL EXAMPLE

To illustrate the analytical results presented above, we consider a specimen of PZT-4, a transversely isotropic piezoelectric ceramic whose material properties are given by Park and Sun [1]. For a through crack with faces perpendicular to the poling direction loaded under remote tension σ^∞ and electric field E^∞ along the poling axis, the symmetry conditions necessary for (20) and (23) are satisfied. By setting G equal to a critical toughness value, we can determine the failure stress σ_{cr}^∞ as a function of the applied field. This function is plotted in Fig. 2(a) for a linear material with a crack of half-length $a = 1\,\mathrm{mm}$ and a critical stress at zero external field of 5 MPa. The insulated case ($\bar{\varepsilon} = 0$) is shown together with the results for an air-filled crack ($\bar{\varepsilon} = \bar{\varepsilon}_0$). The techniques described above can be extended to the case of a slender elliptical void. Figure 2(a) includes results for air-filled voids with a range of initial aspect ratios ρ_0 (ratio of minor axis to major axis). It is evident that the energy release rate for a linear material is dominated by a term that is quadratic in E^∞, giving rise to the nearly even functions depicted in Fig. 2(a). The permeable boundary condition weakens the electrical singularity, thereby reducing the effect of electric field on failure

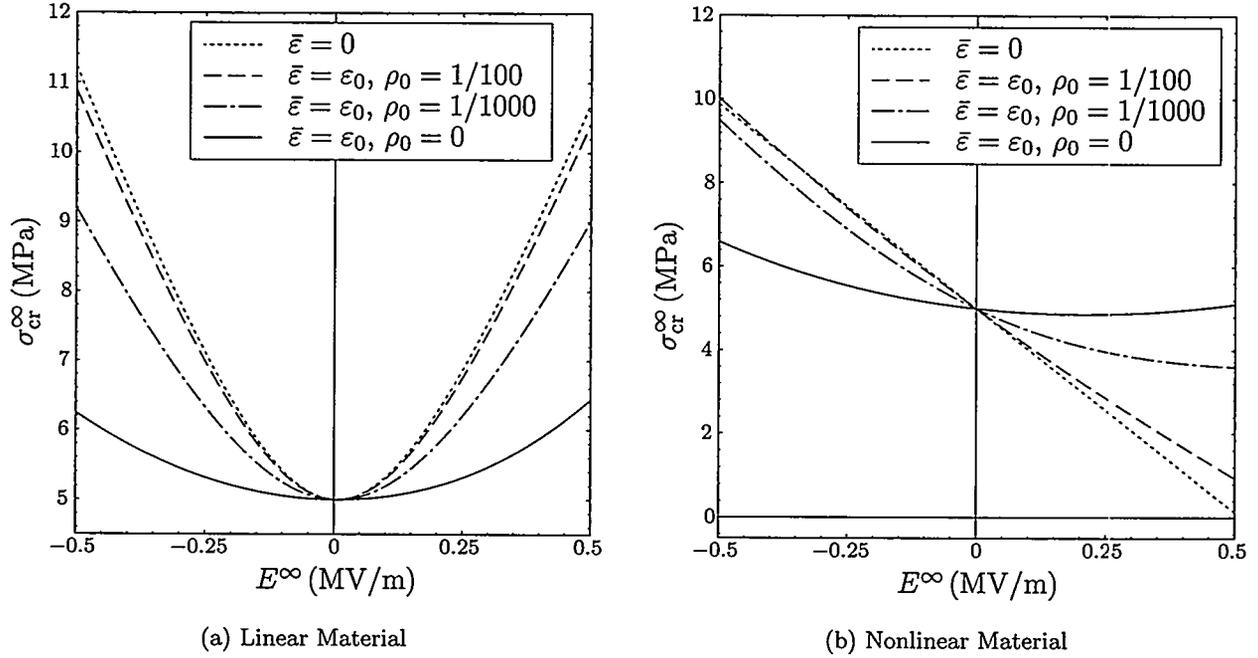(a) Linear Material   (b) Nonlinear Material

Figure 2: Failure Stress *vs.* Applied Field.

load, but the character of the dependence is unchanged. The curves illustrate that the weakening effect is significant for slit cracks ($\rho_0 = 0$) or extremely slender initial voids, but that the insulated condition is a reasonable approximation for void aspect ratios of 1/100 or greater.

The dependence of failure stress on applied field obtained for a nonlinear material using the discrete dipole model is shown in Fig. 2(b). In this case the critical load is dominated by a linear function of electric field with negative slope. As before the permeability of the crack interior tempers the effect of the applied field, while leaving the nature of the dependence largely unchanged.

CONCLUSIONS

A comparison of the two graphs in Fig. 2 clearly demonstrates the importance of considering the material microstructure when making predictions of failure. By adopting a multiscale framework, we isolate the essential features of the microstructure that govern electrical nonlinearity, namely domain switching and polarization saturation. Using discrete electric dipoles to represent this complicated behavior, we arrive at closed-form expressions for the crack driving force that are independent of the details of the ferroelectric switching characteristics. For transversely isotropic piezoceramics, the theory predicts a decrease in failure strength with increasing electric field, matching the trends observed in both indentation and tension tests. A realistic treatment of the crack-face boundary conditions indicates that the permeability of air tempers the electric field dependence, but this effect is only significant for very slender initial defects.

The constraint of using a single dipole to capture all of the material nonlinearity is of course rather restrictive. As a next step, the possibility of allowing a general distribution of dipoles off the crack plane needs to be investigated.

40

ACKNOWLEDGEMENTS

REFERENCES

[1] S. B. Park and C. T. Sun. Fracture criteria for piezoelectric ceramics. *J. Am. Ceram. Soc.*, 78:1475–1480, 1995.

[2] A. G. Tobin and Y. E. Pak. Effects of electric fields on fracture behavior of PZT ceramics. In V. K. Varadan, editor, *Smart Materials*, volume 1916 of *Proc. SPIE*, pages 78–86, Bellingham, Washington, 1993. SPIE.

[3] Z. Suo, C.-M. Kuo, D. M. Barnett, and J. R. Willis. Fracture mechanics for piezoelectric ceramics. *J. Mech. Phys. Solids*, 40:739–765, 1992.

[4] H. Sosa. On the fracture mechanics of piezoelectric solids. *Int. J. Solids Structures*, 29:2613–2622, 1992.

[5] Y. E. Pak. Linear electro-elastic fracture mechanics of piezoelectric materials. *Int. J. Fract.*, 54:79–100, 1992.

[6] Y. E. Pak and A. Tobin. On electric field effects in fracture of piezoelectric materials. In *Mechanics of Electromagnetic Materials and Structures*, AMD-vol. 161/MD-vol. 42, pages 51–62, New York, 1993. ASME.

[7] T.-Y. Zhang, C.-F. Qian, and P. Tong. Linear electro-elastic analysis of a cavity or a crack in a piezoelectric material. *Int. J. Solids Structures*, 35:2121–2149, 1998.

[8] R. M. McMeeking. Towards a fracture mechanics for brittle piezoelectric and dielectric materials. 1998. Submitted for publication.

[9] C. C. Fulton and H. Gao. Effect of local polarization switching on piezoelectric fracture. 1999. Submitted for publication.

[10] A. N. Stroh. Dislocations and cracks in anisotropic elasticity. *Phil. Mag.*, 3:625–646, 1958.

[11] D. M. Barnett and J. Lothe. Dislocations and line charges in anisotropic piezoelectric insulators. *Phys. Stat. Sol. (b)*, 67:105–111, 1975.

[12] C. C. Fulton and H. Gao. Electrical nonlinearity in fracture of piezoelectric ceramics. In L. A. Godoy, M. Rysz, and L. E. Suarez, editors, *MECHANICS PAN-AMERICA 1997*, volume 50 of *Appl. Mech. Rev.*, pages S56–S63, New York, 1997. ASME.

[13] J. D. Eshelby. Elastic inclusions and inhomogeneities. In I. N. Sneddon and R. Hill, editors, *Progress in Solid Mechanics*, volume II, chapter III, pages 87–140. North-Holland Pub. Co., Amsterdam, 1961.

[14] W. F. J. Deeg. *The Analysis of Dislocation, Crack, and Inclusion Problems in Piezoelectric Solids*. PhD thesis, Stanford University, Stanford, California, 1980.

THEORY OF SMALL ANGLE NEUTRON SCATTERING FROM NANODROPLET AEROSOLS

Gerald Wilemski

Department of Physics and Cloud and Aerosol Sciences Laboratory,
University of Missouri-Rolla, Rolla, Missouri 65409, USA

ABSTRACT

The kinematical theory of two body scattering is recast into a form convenient for interpreting small angle neutron scattering (SANS) from crossed beams of neutrons and rapidly moving aerosol particles. Based on a theoretical analysis of the scattered intensity in the Guinier region, a method for determining the particle velocity directly from the experimental data is outlined.

INTRODUCTION

Small angle neutron scattering (SANS) is an important technique for measuring the size and structure of nanoparticles. This information can add much to our detailed understanding of many different aerosol formation processes. One often studied example is the generation of liquid droplet aerosols by homogeneous nucleation and condensation in a supersaturated vapor. The kinetics of the collapse of such metastable states is of great interest for both fundamental and practical reasons. To use SANS to study this process one must overcome the inherent instability of the aerosol over the long time periods needed for the measurements. In one approach to this problem, supersonic nozzle expansions have recently been used to generate a steady aerosol flow directly in the path of the neutron beam. [1, 2]

The analysis of these crossed-beam scattering measurements depends on the resolution of an interesting complication stemming from the relative motion of the neutrons and aerosol particles. The aerosol particles in these experiments are massive, typically containing more than 10^4 water molecules. The nozzle flow field is essentially one-dimensional, and the mean particle velocity normal to the flow direction is less than 1% of the flow velocity. Consequently, for scattering orthogonal to the flow direction, the aerosol particles are effectively stationary while for scattering along or against the flow direction, the high speed particles produce larger neutron momentum transfers. In effect, the momentum of the scattered neutrons is Doppler shifted along the direction of particle motion, and the resulting laboratory scattering patterns are anisotropic. As shown later, this Doppler shift can be used to directly measure the particle speed by means of a suitable Guinier analysis.

Guinier analysis of neutron scattering intensity curves is a standard technique yielding valuable information about the size and number density of the scattering objects. To carry out such an analysis, one plots the logarithm of the scattered intensity versus the square of the momentum transfer wave vector, q. At small q the plot is linear with a slope that is directly proportional to r_G^2, where r_G is the radius of gyration of the scatterers. In the present case, the slope also contains valuable information about the particle speed, as explained below. The intercept is proportional to the number density of scatterers N and the mean square

volume of the scatterers. With proper interpretation of these data, the aerosol size distribution can then be deduced from the full scattering curve as shown elsewhere. [1, 2]

To properly interpret the measured scattered intensity, it is necessary to relate the differential scattering cross sections for the center of mass (COM) frame and the laboratory (LAB) frames. This task requires that q, the momentum transfer wave vector, be expressed in terms of laboratory variables and parameters for the appropriate scattering geometry. It also involves properly accounting for the differences in solid angles subtended at the detector by the scattered neutrons as viewed in the COM and LAB frames. Both of these exercises have been carried out previously in the context of crossed molecular beam scattering [3, 4], but for detector geometries different from the one used in the aerosol experiments. In the Appendix, the necessary results will be independently derived in a form directly applicable to these experiments.

In the main body of the paper, the equations for the scattered neutron intensity for a stationary aerosol are presented first. Then the key equations relating the LAB and COM scattered intensities for a flowing aerosol are developed. These equations also provide the basis for determining the aerosol particle speed by a Guinier analysis of the scattered intensity. The paper concludes with a summary and the Appendix.

SCATTERED INTENSITY IN THE ABSENCE OF FLOW

Consider a set of particles suspended in a scattering volume V with no net flow velocity in V. For a collection of m different types of particles with n_α particles of type α, the total scattered intensity per unit scattering volume, I_0 (units: cm^{-1}), may be written as [5, 6]

$$I_0(q) = V^{-1} \left\langle \left| \sum_{\alpha=1}^{m} \sum_{j=1}^{n_\alpha} f_\alpha(\mathbf{q}) \exp(i\mathbf{q} \cdot \mathbf{r}_{j\alpha}) \right|^2 \right\rangle, \tag{1}$$

where $\mathbf{q}$ is the momentum transfer wave vector, $\mathbf{r}_{j\alpha}$ is the center of mass position vector of particle j of type α, and the angle brackets denote an average over all particle positions with an appropriate configuration space distribution function. The form amplitude $f_\alpha(\mathbf{q})$ for scattering by a particle of type α is given by the expression,

$$f_\alpha(\mathbf{q}) = \int_{V_\alpha} \rho_\alpha(\mathbf{r}) \exp(i\mathbf{q} \cdot \mathbf{r}) d\mathbf{r}, \tag{2}$$

where $\mathbf{r}$ is measured from the center of mass of the particle and the integral extends over the particle volume V_α. The quantity $\rho_\alpha(\mathbf{r})$ is the scattering length density for a particle of type α. As indicated by its argument, ρ_α may vary with position, and its specific spatial dependence should account for particle shape, the distributions of different molecular species within the particle, and the diffuseness of the interfacial region. The validity of Eq.(1) rests on the first Born approximation, which in effect neglects multiple scattering events. In the present application, the total volume fraction of aerosol particles is $<10^{-5}$, and the total number density N of particles is on the order of 10^{12} cm^{-3}, so multiple scattering is negligible.

The total scattered intensity contains contributions from both intraparticle scattering and interparticle correlations. This may be seen by expanding the product of sums in Eq.(1) to obtain after some simplifications and neglect of 1 with respect to n_α:

$$I_0(q) = \sum_{\alpha=1}^{m} N_\alpha \left\langle f_\alpha^2(\mathbf{q}) \right\rangle + \sum_{\alpha=1}^{m} N_\alpha n_\alpha \left\langle f_\alpha^2(\mathbf{q}) \exp(i\mathbf{q} \cdot \mathbf{r}_{12}) \right\rangle + \sum_{\alpha \neq}^{m} \sum_{\beta=1}^{m} N_\alpha n_\beta \left\langle f_\alpha(\mathbf{q}) f_\beta^*(\mathbf{q}) \exp(i\mathbf{q} \cdot \mathbf{r}_{\alpha\beta}) \right\rangle, \tag{3}$$

where N_α is the number density of type α particles, $N_\alpha = n_\alpha/V$, $\mathbf{r}_{12}$ is the separation vector between two particles of type α, $\mathbf{r}_{\alpha\beta}$ is the separation vector between a particle of type α and one of type β, and $*$ denotes the complex conjugate. In this expression, the first sum represents scattering from individual particles, the second accounts for interferences between two different particles of the same type, and the third for interferences between two different types of particles, $\alpha \neq \beta$. Because the aerosols under consideration here are so dilute, typical values of r_{12} and $r_{\alpha\beta}$ will be about 10^3 nm. Thus, the main contribution from the

interparticle interference terms should occur at values of q two orders of magnitude smaller than those of experimental interest. [1, 2] Reinforcement for the notion that small interparticle distances are relatively rare comes from two other factors. First, due to the massive size of the particles, mean interparticle speeds are very small, typically 1–4 m/s, and particle collision frequencies are low, about 5000/s or smaller. Moreover, if the particles are liquid as in the experiments of immediate concern [1, 2], any infrequent, direct collisions result in the replacement of a particle pair by a slightly larger single particle. Second, the particles form by means of homogeneous nucleation in a supersaturated vapor, and the probability for two such density fluctuations to occur simultaneously in close proximity is quite small. Furthermore, a rapidly growing droplet locally depresses the condensible vapor concentration further lowering the chances for subsequent nucleation near an existing particle.

Thus, the scattered intensity should be very well approximated by just the contributions from individual particles, and Eq.(3) reduces to

$$I_0(q) = \sum_\alpha N_\alpha P_\alpha(q), \tag{4}$$

with the identification of $\langle f_\alpha^2(\mathbf{q}) \rangle$ as the particle form factor $P_\alpha(q)$. After Eq.(2) is substituted for $f_\alpha(\mathbf{q})$, $P_\alpha(q)$ can be written as

$$P_\alpha(q) = \left\langle \int_{V_\alpha'} \int_{V_\alpha''} \rho_\alpha(\mathbf{r}')\rho_\alpha(\mathbf{r}'') \exp(i\mathbf{q}\cdot\mathbf{r})d\mathbf{r}'d\mathbf{r}'' \right\rangle, \tag{5}$$

where $\mathbf{r} = \mathbf{r}' - \mathbf{r}''$ and the angle brackets now represent a random average over all orientations of $\mathbf{r}$ with respect to $\mathbf{q}$. After the averaging is carried out, $P_\alpha(q)$ simplifies to the following general form,

$$P_\alpha(q) = \int_{V_\alpha'} \int_{V_\alpha''} \rho_\alpha(\mathbf{r}')\rho_\alpha(\mathbf{r}'') \frac{\sin qr}{qr} d\mathbf{r}'d\mathbf{r}'', \tag{6}$$

which is still independent of any assumptions about particle shape, composition or structure.

For a spherical particle of radius R with a sharp boundary and a uniform composition, Eq.(6) reduces to the well-known result

$$P(q, R) = 16\pi^2(\rho_b)^2(\sin qR - qR\cos qR)^2/q^6, \tag{7}$$

where ρ_b is the constant scattering length density of the particle.

SCATTERED INTENSITY WITH FLOW

The aerosol particles are now assumed to move with a speed v_p in the positive x direction of a right-handed, 3-dimensional, LAB-fixed, Cartesian coordinate system with the scattering volume at the origin. Neutrons, moving with speed v_n, approach the particles from the negative z direction and are scattered into the forward z direction. The scattering direction in the LAB frame is defined by the polar angle θ with respect to the LAB z-axis, which is also the usual LAB scattering angle, and by the azimuthal scattering angle ϕ, measured from the x-axis in the detector plane. For this right-angle crossed beam geometry, as shown in the Appendix, the LAB scattered intensity I is related to the scattered intensity I_0 in the COM frame by the equation

$$I(q) = I_0(q_0) \frac{(\xi + \sqrt{1 + \xi^2})^2}{\sqrt{1 + \xi^2}}, \tag{8}$$

where

$$\xi = (v_p/v_n)\sin\theta\cos\phi. \tag{9}$$

The momentum transfer wave vectors, q and q_0, in the respective LAB and COM frames, are equal and are expressed in laboratory variables as

$$q^2 = q_0^2 = 2k^2[1 + (\xi - \cos\theta)(\xi + \sqrt{1 + \xi^2})], \tag{10}$$

44

where the incident neutron wave vector k is related to the neutron wavelength λ in the usual way,

$$k = 2\pi/\lambda. \tag{11}$$

Equations (8)-(10) are valid for the elastic scattering of neutrons by very massive aerosol particles, and they form the basis for the data analysis algorithm for the results of aerosol SANS experiments. [1, 2] An important component of that algorithm is a Guinier analysis of the small q behavior of $I(q)$, which is discussed next.

For fixed λ, small q is equivalent to very small values of θ and, hence ξ, since the velocity ratio v_p/v_n never exceeds 2 in our experiments. Thus, we proceed by expanding Eqs.(8) and (7) for small values of q and ξ to obtain in lowest order,

$$I(q) = I(0)[1 + q^2 r_G^2/3][1 + 2\xi + 3\xi^2/2], \tag{12}$$

where the scattered intensity at $q = 0$ is

$$I(0) = (4\pi\rho_b/3)^2 N\langle r^6\rangle, \tag{13}$$

the radius of gyration is

$$r_G^2 = \frac{3}{5}\langle r^8\rangle/\langle r^6\rangle, \tag{14}$$

N is the total number density of aerosol particles,

$$N = \sum_j N(r_j), \tag{15}$$

and the mean values are defined as

$$N\langle r^n\rangle = \sum_j (r_j)^n N(r_j). \tag{16}$$

Since q itself depends on the as yet unknown particle velocity, it is not a useful independent variable. To surmount this difficulty, we expand Eq.(10) for small θ to find

$$q^2 = q_i^2(1 + \xi + (v_p/v_n)^2 \cos^2\phi), \tag{17}$$

where q_i is the nominal momentum transfer wave vector based on the incident (i) neutron wavelength,

$$q_i = (4\pi/\lambda)\sin(\theta/2). \tag{18}$$

One can also think of q_i as the value of q for stationary aerosol particles ($v_p = 0$). After combining Eqs.(12) and (17) and retaining only terms that are constant or linear in ξ, we obtain

$$\frac{I(q)}{I(0)} = 1 + 2\xi + \frac{q_i^2 r_G^2}{3}(1 + 3\xi + (1 + 2\xi)(\frac{v_p}{v_n}\cos\phi)^2). \tag{19}$$

This result displays explicitly the velocity dependence of the scattered intensity at small q. It is valid for $r_G^2 \gg \lambda^2$. An important feature of this equation is the $\cos^2\phi$ term. It strongly affects the shape of the anisotropic scattering pattern, and it also determines the slope in Guinier plots based on data point averaging procedures that eliminate odd powers of $\cos\phi$. To complete the Guinier analysis, we consider three types of averages.

First, we take a circular average over the azimuthal angle ϕ at constant θ (or q_i). We denote the result as $\bar{I}(q_i)$, expand its natural logarithm, and retain only the term quadratic in q_i to put the result in standard form,

$$\ln\bar{I}(q_i) = \ln I(0) + q_i^2 r_G^2(1 + (v_p/v_n)^2/2)/3. \tag{20}$$

Next, we take a "horizontal" average, denoted as I_h, by averaging pairs of intensities at $\phi = 0$ and π to find

$$\ln I_h(q_i) = \ln I(0) + q_i^2 r_G^2 (1 + (v_p/v_n)^2)/3. \tag{21}$$

Finally, we take a similar "vertical" average, denoted as I_v, by averaging pairs of intensities at $\phi = \pm\pi/2$ to find

$$\ln I_v(q_i) = \ln I(0) + q_i^2 r_G^2/3. \tag{22}$$

These results show that the velocity dependence of the apparent Guinier slope depends on the type of average taken, but in each case this velocity dependence arises solely from the q^2 term of Eq. (12) with Eq.(17) since only even powers of $\cos\phi$ survive the averaging done here. In other words, the geometric and flux correction factor that multiplies I_0 in Eq.(8) does not contribute to these results, provided $r_G^2 \gg \lambda^2$. This condition is satisfied in recent experiments [1, 2], since $r_G/\lambda \sim 8$. By ratioing the values of these slopes it is possible to determine, by direct experimental means, the particle velocity. This has recently been done [2], and the results were in very good agreement with independent estimates of particle velocity based on gasdynamic measurements.

SUMMARY AND CONCLUSIONS

The kinematic theory of two body scattering has been cast into a form that is well-suited for application to a crossed beam scattering geometry. This theoretical framework is essential for the proper interpretion of experimental aerosol SANS data and for deriving accurate particle size distributions. Furthermore, with accurate measurements in the low q region, the theory provides the means to exploit the anisotropy in the scattered intensity to measure the actual particle velocity.

APPENDIX

Our goal here is to relate the scattering intensities in the COM and LAB frames using scattering angles and parameters appropriate for the crossed beam scattering and detector geometries used in our experiments. Much of Sears's [7] notation will be used, and his kinematic analysis will be augmented to account for the motion of the target particle.

The absolute scattered neutron intensity in the LAB frame, $I(\theta, \phi)$, is defined as

$$I(\theta, \phi) = \frac{1}{V}\frac{d\sigma}{d\Omega}, \tag{A1}$$

where θ is the usual LAB scattering angle, ϕ is the azimuthal scattering angle measured in the detector plane, V is the scattering volume, and $d\sigma/d\Omega$ is the differential scattering cross section for the aerosol particles measured in the LAB frame. Note that as defined here, σ is directly proportional to the total number of aerosol particles in V. Thus, the quantity $I(\theta, \phi)d\Omega$ represents the total number of neutrons scatterered into the differential solid angle $d\Omega(\theta, \phi)(= \sin\theta d\theta d\phi)$ normalized by the scattering volume and the incident neutron flux J. With these definitions, I corresponds directly to the absolute scattering intensity (units: cm^{-1}) found experimentally.

In the LAB frame, the neutrons and aerosol particles are moving, respectively, with velocities $\mathbf{v}_n$ and $\mathbf{v}_p$ before the collision, and J simply equals the product of the average number density of neutrons in the beam, n, and the LAB neutron speed

$$J = nv_n = n|\mathbf{v}_n|. \tag{A2}$$

Let us designate quantites in the COM frame with the subscript "0". Then because the absolute number of scattered neutrons in the two frames must be identical, we can write

$$J\frac{d\sigma}{d\Omega}d\Omega = J_0\frac{d\sigma_0}{d\Omega_0}d\Omega_0, \tag{A3}$$

where J_0 depends on v, the relative speed of the neutrons and aerosol particles,

$$J_0 = nv = n|\mathbf{v}_n - \mathbf{v}_p|. \tag{A4}$$

To relate I and I_0, we combine Eq.(A1) and Eq.(A3) to find,

$$I = I_0 \frac{J_0}{J} \frac{d\Omega_0}{d\Omega}, \tag{A5}$$

where

$$I_0 = \frac{1}{V} \frac{d\sigma_0}{d\Omega_0}. \tag{A6}$$

Equation (A5) is useful because for spherical aerosol particles the COM differential scattering cross section is isotropic and I_0 is only a function of θ_0, the COM scattering angle. It is, therefore, relatively easy to calculate. To use Eq.(A5) it is necessary to express θ_0 in terms of LAB variables and to evaluate $d\Omega_0/d\Omega$. To do this, we use an algebraic approach based on the conservation of momentum and energy.

The analysis will be carried out using wave vectors, $\mathbf{k}$ and $\mathbf{K}$, of the neutrons and aerosol particles, respectively, rather than their respective velocities, $\mathbf{v}_n$ and $\mathbf{v}_p$. In the LAB frame, the wave vectors are defined as

$$\hbar\mathbf{k} = m_n \mathbf{v}_n, \tag{A7}$$

and

$$\hbar\mathbf{K} = m_p \mathbf{v}_p, \tag{A8}$$

where m_n and m_p are the neutron and particle masses, respectively, and $\hbar$ is Planck's constant divided by 2π. If we use a prime to denote values after the collision, the conservation of momentum and energy are simply expressed as

$$\mathbf{k} + \mathbf{K} = \mathbf{k}' + \mathbf{K}', \tag{A9}$$

and

$$\frac{k^2}{m_n} + \frac{K^2}{m_p} = \frac{(k')^2}{m_n} + \frac{(K')^2}{m_p}. \tag{A10}$$

In the COM frame, the scattering problem reduces to the motion of a single particle with reduced mass μ,

$$\mu = m_n m_p / (m_n + m_p), \tag{A11}$$

with wavevectors $\mathbf{k}_0$ and $\mathbf{k}_0'$ before and after the collision,

$$\frac{\mathbf{k}_0}{\mu} = \frac{\mathbf{k}}{m_n} - \frac{\mathbf{K}}{m_p}, \tag{A12}$$

$$\frac{\mathbf{k}_0'}{\mu} = \frac{\mathbf{k}'}{m_n} - \frac{\mathbf{K}'}{m_p}. \tag{A13}$$

To evaluate $d\Omega_0/d\Omega$, we borrow an argument from Sears (p. 31). [7] First, we substitute Eq.(A9) into Eq.(A13) to obtain

$$\mathbf{k}_0' = \mathbf{k}' - \mu(\mathbf{k} + \mathbf{K})/m_p. \tag{A14}$$

Since $\mathbf{k}$ and $\mathbf{K}$ are constant vectors, any change in $\mathbf{k}'$ produces a corresponding change in $\mathbf{k}_0'$, and the differential wave vector volume elements d^3k' and d^3k_0' must be equal. If we use spherical coordinates appropriate to the LAB and COM frames, this equality takes the form,

$$(k')^2 dk' d\Omega = (k_0')^2 dk_0' d\Omega_0, \tag{A15}$$

from which we see that

$$\frac{d\Omega_0}{d\Omega} = \left(\frac{k'}{k_0'}\right)^2 \frac{dk'}{dk_0'}. \tag{A16}$$

The next step is to express k' and k_0' in terms of k and K, the incident neutron and particle momenta in the LAB frame. To do this, we first use Eq.(A9) to form the dot product of K' with itself. After substituting this result into Eq.(A10) and noting that for our right-angle crossed beam and detector geometries,

$$\mathbf{k} \cdot \mathbf{K} = 0, \tag{A17}$$

$$\mathbf{k} \cdot \mathbf{k}' = kk' \cos\theta, \tag{A18}$$

and

$$\mathbf{k}' \cdot \mathbf{K} = k'K \sin\theta \cos\phi, \tag{A19}$$

we find a quadratic equation for k' that yields the physical root,

$$k' = \kappa + \left(\kappa^2 + uk^2\right)^{1/2}, \tag{A20}$$

where

$$\kappa = (\mu/m_p)(k\cos\theta + K\sin\theta\cos\phi), \tag{A21}$$

and

$$u = (m_p - m_n)/(m_n + m_p). \tag{A22}$$

Next, from Eq.(A14) and (A17) we obtain

$$(k_0')^2 = (k')^2 - 2k'\kappa + (\mu/m_p)^2(k^2 + K^2), \tag{A23}$$

from which it follows that

$$k_0'\frac{dk_0'}{dk'} = k' - \kappa. \tag{A24}$$

Equations (A16) and (A24) are equivalent to earlier results obtained mainly by geometric arguments. [3, 4] Finally, with the help of Eq.(A16), (A20), and (A24), Eq.(A5) can be expressed as

$$I = I_0\frac{J_0}{J}\left(\frac{k'}{k_0'}\right)^2\frac{k_0'}{\sqrt{\kappa^2 + uk^2}}. \tag{A25}$$

To simplify this further, we first note that for elastic collisions, energy conservation in the COM frame implies that

$$k_0' = k_0. \tag{A26}$$

This result may also be demonstrated explicitly using Eq.(A9), (A10), (A12), and (A13). By combining Eq.(A2), (A4), (A7) and (A12), we can also express the LAB and COM neutron fluxes in terms of k and k_0,

$$J = \hbar nk/m_n, \tag{A27}$$

and

$$J_0 = \hbar nk_0/\mu. \tag{A28}$$

Using the last three simple relations, Eq.(A25) can be rewritten as

$$I = I_0\frac{m_n}{\mu}\left(\frac{k'}{k}\right)^2\frac{k}{\sqrt{\kappa^2 + uk^2}}, \tag{A29}$$

which is an exact result for elastic scattering that is limited only by the assumption of a specific geometry for the incident neutron and particle beams ($\mathbf{k} \cdot \mathbf{K} = 0$). This assumption can easily be relaxed if desired.

With the help of Eq.(A7), (A8), (A20), and (A21), Eq.(A29) provides all of the geometric corrections needed to understand the laboratory scattering intensity. What remains is to treat the additional anisotropy that arises when I_0 is expressed as a function of laboratory variables. As noted earlier, scattering in the COM frame is isotropic, depending only on the COM scattering angle θ_0, but θ_0 itself is a function of

48

both laboratory scattering angles. For the systems under consideration here, I_0 is only a function of q_0, the magnitude of the momentum transfer wave vector $\mathbf{q_0}$, defined as

$$\mathbf{q_0} = \mathbf{k_0} - \mathbf{k_0'}. \qquad (A30)$$

From Eq.(A30), (A7), (A8), (A12), and the definition of θ_0,

$$\mathbf{k_0} \cdot \mathbf{k_0'} = k_0^2 \cos\theta_0, \qquad (A31)$$

it follows that

$$k_0 = \mu v/\hbar, \qquad (A32)$$

and

$$q_0 = 2k_0 \sin(\theta_0/2). \qquad (A33)$$

Thus, q_0 depends on the reduced mass and the relative speed v $(= \sqrt{v_n^2 + v_p^2})$ of the neutrons and aerosol particles.

To express q_0 in terms of the laboratory scattering angles, we substitute Eq.(A12) and (A13) into Eq.(A30) and use Eq.(A9) to eliminate $\mathbf{K}$ and $\mathbf{K'}$. The result, which is readily apparent on physical grounds, is that the momentum transfer wave vector in the LAB frame $\mathbf{q}$ is identical to $\mathbf{q_0}$

$$\mathbf{q_0} = \mathbf{q} = \mathbf{k} - \mathbf{k'}. \qquad (A34)$$

We next evaluate q^2 from Eq.(A34) with the help of Eq.(A18), (A20), and (A21) to obtain

$$q^2 = k^2[1 + u + 2(\xi - \cos\theta)(\xi + (u + \xi^2)^{1/2})], \qquad (A35)$$

where

$$\xi = \kappa/k. \qquad (A36)$$

An explicit functional relationship between the COM (θ_0) and LAB (θ, ϕ) scattering angles is readily obtained by equating q_0 (Eq.(A33)) with q (Eq.(A35)). In the special case of stationary target particles, this relationship reduces to the well-known result, $\tan\theta = \sin\theta_0/(\cos\theta_0 + m_n/m_p)$. [8]

When we work in the massive particle limit, $m_p >> m_n$, which is appropriate in the present situation, we find that $u = 1$ and ξ reduces to

$$\xi = (v_p/v_n)\sin\theta\cos\phi. \qquad (A37)$$

In this limit, Eqs.(A29) and (A35) simplify to the results presented in Eq.(8)–(10). With Eq.(A37), it is also easy to see that the Doppler shift in scatterered neutron momentum vanishes for scattering orthogonal to the direction of particle motion $(\phi = \pm\pi/2)$.

ACKNOWLEDGEMENT

REFERENCES

1. B. E. WYSLOUZIL, J. L. CHEUNG, G. WILEMSKI, and R. STREY, *Phys. Rev. Lett.* <u>79</u>, 431 (1997).

2. B. E. WYSLOUZIL, G. WILEMSKI, J. L. CHEUNG, R. STREY, and J. BARKER, *Phys. Rev. E*, submitted (1999)

3. F. A. MORSE and R. B. BERNSTEIN, *J. Chem. Phys.* <u>37</u>, 2019 (1962).

4. R. K. B. HELBING, *J. Chem. Phys.* <u>48</u>, 472 (1968).

5. R. KLEIN and B. D'AGUANNO in *Light Scattering, Principles and Development*, edited by W. Brown, Clarendon Press, Oxford (1996) p. 30.

6. J. S. HIGGINS and H. C. BENOIT, *Polymers and Neutron Scattering*, Clarendon Press, Oxford (1994).

7. V. F. SEARS, *Neutron Optics*, Oxford, New York (1989).

8. H. GOLDSTEIN, *Classical Mechanics, 2nd ed.*, Addison-Wesley, Reading, Massachusetts (1980).

PHASE-DEFECT DESCRIPTION OF TRAVELING-WAVE CONVECTION

C. M. Surko* and A. La Porta

Department of Physics, University of California, San Diego
La Jolla CA 92093

ABSTRACT

Convection is studied in a horizontal layer of a binary fluid mixture of ethanol and water. In this mixture, the coupling between the temperature and concentration fields leads to dynamical behavior not observed in pure fluids. Convection takes the form of traveling waves, and the system provides a useful model for studying traveling-wave phenomena in non-equilibrium systems. Studies are described of the relaxation of turbulent traveling-wave states, which is a kind of phase turbulence. The evolution of the patterns can be described in terms of topological defects in the phase field. Work toward the development of a predictive model of the dynamics of the system in terms of these phase defects is described.

I. INTRODUCTION

Most natural phenomena and many commercial and industrial processes occur in systems driven far from thermodynamic equilibrium. The many and diverse examples include weather patterns, ocean flows, biological systems, heat transfer, crystal growth and laser operation.[1-7] Nontrivial spatial structures and dynamics frequently arise in these systems and can influence such quantities as the transport of heat, material, and momentum. While the mechanisms responsible for these phenomena are understood at the microscopic level (e.g., using the Schrodinger or Navier Stokes equations), predicting the self organization and dynamics on larger length scales is not presently possible. The similarity of the patterns that are formed in very diverse settings provides evidence that there is a certain kind of universality in these phenomena.[8,9] The objective of the research described here is to develop an understanding of the underlying principles that determine such patterns and dynamics in systems driven far from equilibrium.

The patterns and dynamics generated in a binary fluid mixture subject to thermal forcing provide a useful model system to study an important range of traveling-wave phenomena.[10-14] This is

50

variant of Rayleigh-Bénard convection, in which horizontal layer of fluid that is confined between material walls and is heated from below. The temperature difference, ΔT, across the layer is typically expressed in dimensionless form as the Rayleigh number, $R = g\alpha h^3 \Delta T / \nu\kappa$, where g is the acceleration of gravity, h is the height of the layer, α is the thermal expansion coefficient, ν is the kinematic viscosity, and κ is the thermal diffusivity of the fluid.[9] In this paper, ΔT is expressed in terms of the reduced Rayleigh number, $r = R/R_c$, where $R_c = 1708$ is the onset of convection in a pure fluid. In mixtures of ethanol and water such as those studied here, heat and concentration can diffuse in the fluid or be advected by the velocity field. In these mixtures, the diffusivity of concentration, D_c, is much slower than that of heat, and the ratio of diffusivities is parameterized by the Lewis number, $L = D_c/\kappa$. Temperature and concentration perturbations influence each other, introducing feedback into the system. The coupling of the concentration current to the temperature gradient is known as the Soret effect and is expressed in terms of the separation ratio, $\Psi = -c(1-c)S_t$ (β/α) where c is the ethanol concentration, S_t is the Soret coefficient, and β is the solutal expansion coefficient.[15] For the work described here, $r \sim 1$ - 3, and $\Psi = -0.24$. The Prandtl number $P_r \sim 10$, and $L \sim 10^{-2}$.

Shown in the figure below are examples of the traveling wave convection patterns observed in this system. The challenge that we address here is to develop an understanding of traveling-wave patterns and dynamics such as those illustrated in this figure.
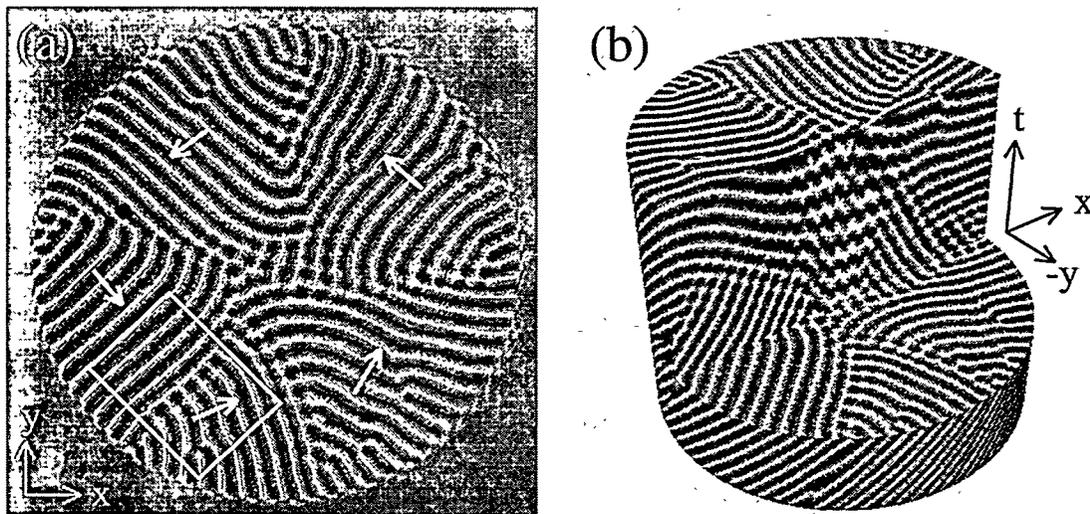

Fig. 1. Experimentally measured traveling wave convection patterns in a large aspect ratio cell. (a) A quasi stationary state at time t_0 with well defined domain boundaries. White arrows indicate the direction of roll propagation. The rolls move in approximately the same direction around the boundary. The white rectangle indicates a "perpendicular boundary, where two traveling-wave domains interact. (b) The spatio-temporal pattern shown as a 3D solid. A section of the cylinder created by the temporal extension of the circular pattern has been cut away to expose part of the interior of the solid volume. The "shelf" shows a portion of the pattern at t_0 and the cylinder extends from $t_0 - 15t$ to $t_0 + 31t$, where t is in units of the thermal diffusion time in the system. The facing surface shows the time evolution of a line through the center of the pattern.

II. DESCRIPTION OF THE EXPERIMENT

The apparatus, which is described in detail elsewhere,[12] consists of a convection cell a diameter of 21 cm and a height, h = 0.4 cm, giving an aspect ratio (Γ=r/h) of 26. In this large aspect ratio cell, the central region of the pattern evolves without strong interaction with the cell boundary. The temperature uniformity is better than 1 mK, representing an estimated peak-to-peak variation in Rayleigh number of 0.02% across the cell. Visualization is accomplished using a white-light shadowgraph. Images are acquired using a CCD camera and digitized with a PC and frame grabber. The evolution of the patterns occurs over periods that are long compared to the vertical thermal diffusion time (τ_θ=h^2/κ=124 s) and the mass diffusion time (τ_C=h^2/D$_c \approx$16,000 s). In this paper distances are expressed in units of h and times in units of τ_θ.

III. COMPLEX ORDER PARAMETER AND PHASE DEFECTS

For TW patterns, a single frame is insufficient to determine the direction of wave propagation. The description we have adopted uses the fact that the 2-D TW patterns and their associated time dependence can be described by a scalar complex order parameter. The time series of a typical point in the pattern oscillates periodically and has a relatively narrow frequency spectrum. Complex demodulation of the time series measured at each pixel is used to determine the amplitude and phase at each pixel in the pattern. Assuming that the time series oscillates at a reasonably well-defined frequency with phase and amplitude modulations, the time sequence at each pixel is of the form $a(\mathbf{x}) = a_\omega(\mathbf{x}, t) \cos(\omega t + \phi_\omega(\mathbf{x}, t))$, where ω is the carrier frequency, and $a_\omega(\mathbf{x}, t)$ and $\phi_\omega(\mathbf{x}, t)$ are the real functions describing the amplitude and phase modulations of the carrier, respectively. The data are multiplied by a complex carrier wave, $e^{i\omega t}$, producing beat components at the sum and difference frequencies. After the high frequency terms are filtered out, the remaining function, the complex order parameter, $A(\mathbf{x}, t)$, is related to the phase and amplitude modulation by $A(\mathbf{x}, t) = (1/2)a_\omega(\mathbf{x}, t) \exp(-i\phi_\omega(\mathbf{x}, t))$. We find that the amplitude, $a_\omega(\mathbf{x}, t)$, varies slowly over the patterns, and so the information is contained in the phase.

With this in mind, we have developed tools to identify topological *phase defects* in the patterns, defined as points at which the amplitude $||A(\mathbf{x})|| = 0$ (i.e., Re(A) = Im(A) = 0). At these points the phase $\phi(\mathbf{x})$ is undefined (i.e., see Fig. 2(a)). The integral $d\phi$ around the defect equals $2\pi c$, where c is the topographical charge of the defect (i.e., c = +1 if the phase advances by 2π and c = -1 if the phase changes by -2π in one circuit clockwise around the defect).[16] In order to specify
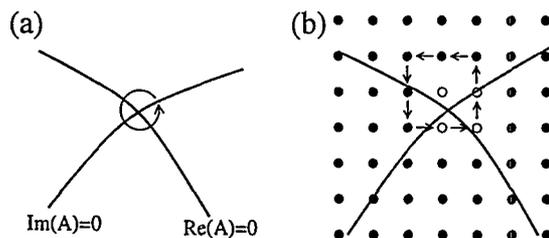

Fig. 2. Sketch of a phase defect: (a) in a continuous field, and (b) in a discrete field. The phase advances by 2π in one excursion clockwise around the defect.

every defect in the pattern, the topological charge at each pixel is calculated using a loop consisting of the eight surrounding pixels, as shown in Fig. 2(b), and then stored in a charge map. Generally, the defects lie between pixels and are contained by loops centered on four adjacent pixels, as indicated by the unshaded lattice points in Fig 2(b). Therefore, we identify any connected group of pixels with the same nonzero topological charge as a single defect. The data presented here are sampled at a resolution of at least 14 pixels per wavelength, and for this sampling rate, the error rate in identifying phase defects is extremely low.

IV. RELAXATION OF TURBULENT STATES

We studied the time development of initially turbulent states to try to determine what characterizes the evolution to more ordered patterns. Disordered states, such as that shown in Fig. 3 (a), were generated by making a sudden jump in Rayleigh number.
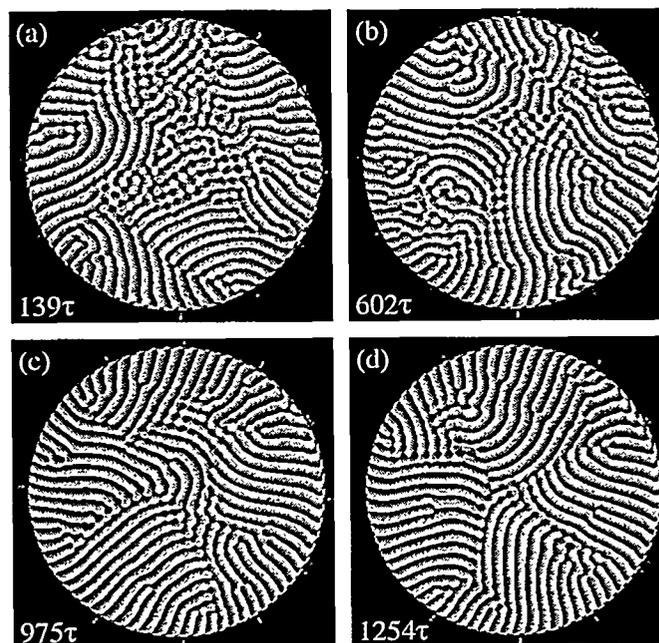

Fig. 3. Traveling-wave convection patterns, represented by the phase of the complex amplitude, at several stages of the evolution of the pattern from a turbulent initial state. The elapsed time from the initiation of convection is given for each of the four images. White to black corresponds to the phase change $0 - 2\pi$.

Fig. 4 shows the contours of the phase fields corresponding to the patterns in Fig. 3 at four times during the relaxation of a pattern. The crossings of $Re(A) = 0$ and $Im(A) = 0$ determine the positions of the phase defects. The resulting arrays of defects, corresponding to the patterns in Fig. 3, are shown in Fig. 5. The motion of the individual defects in Fig. 5 is shown by the gray tails on the defects.

A key question is what determines the characteristic evolution of this pattern from an initially disordered state to a more ordered one and what limits the degree to which the patterns order. As the pattern evolves, the knots of phase contours are found to disentangle themselves, forming an

array of parallel lines that cross the minimum number of times necessary to satisfy the boundary conditions.[13] The end result is a pattern with several large domains of traveling waves, separated by distinct, stable domain boundaries. In the defect description, the annihilation of defect-antidefect pairs results in the minimal number of like-sign defects necessary to satisfy the boundary conditions, leading to mature patterns such as the one shown in Figs. 3 (d) and 4(d).[13]
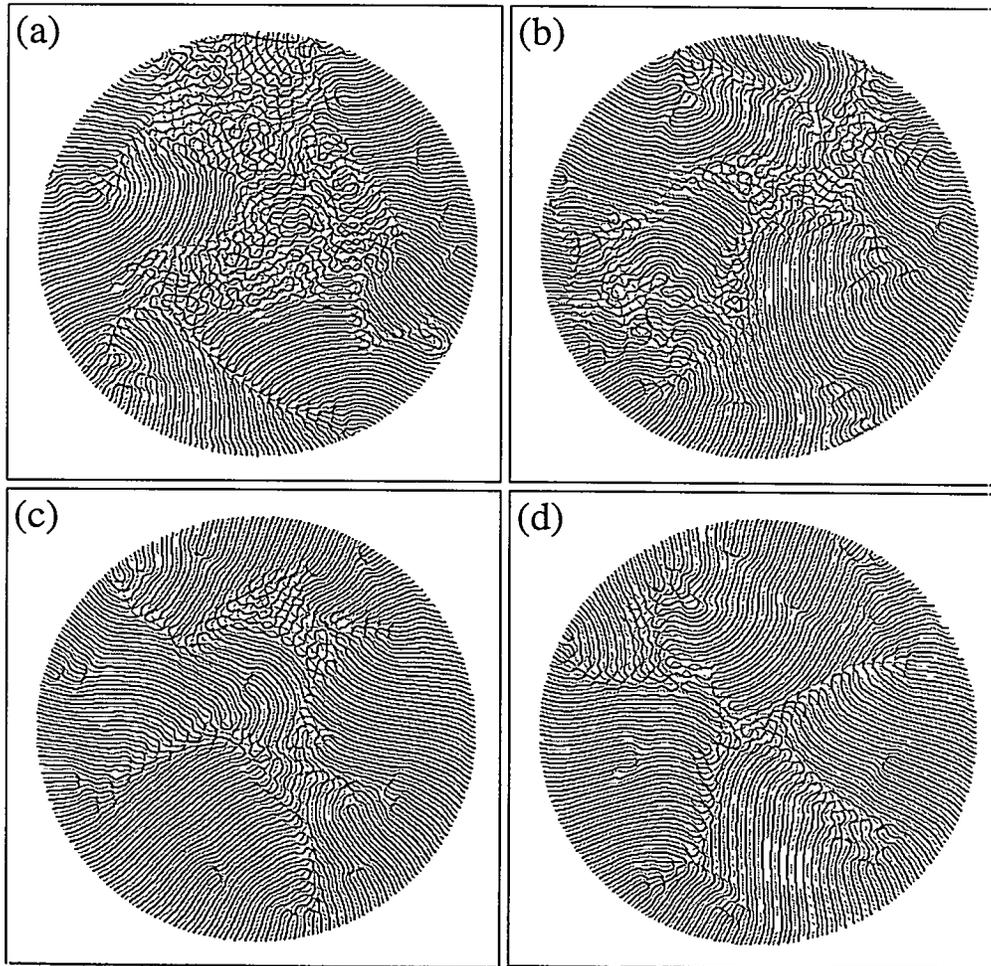

Fig. 4. Contours of Re(A)=0 and Im(A)=0 are marked by black and grey lines for the patterns shown in the four panels of Fig. 3.

We have found that the patterns continue to evolve until the *net* charge grows from the statistical variation in the initial number of defects (e.g., from 20 - 30 out of a total of ~ 600 - 1,000 defects) to a value of approximately 72. This value of 72 is the number of defects that would be expected if all of the rolls at the cell boundary orient perpendicular to the boundary. In this case, each roll pair terminates within the pattern, which is the configuration observed in our experiments. We concluded that the guiding principle that determines the pattern evolution is the dominance of the long-range effect of the cell boundaries. Rolls orient approximately perpendicular to the cell walls, and sources of traveling waves are unstable. Thus all waves travel in the same direction, resulting in global rotation of the pattern. The net charge of 72

corresponds to defects located predominantly in perpendicular boundaries [e.g., see the white rectangle in Fig. 1 (a)] with a few isolated dislocations. The remainder of the defects (i.e., the total defect number ~ 120) occur mainly in small regions of so-called "cross roll instability," which in the defect picture are regions comprised of ordered square lattices of defects of opposite sign.
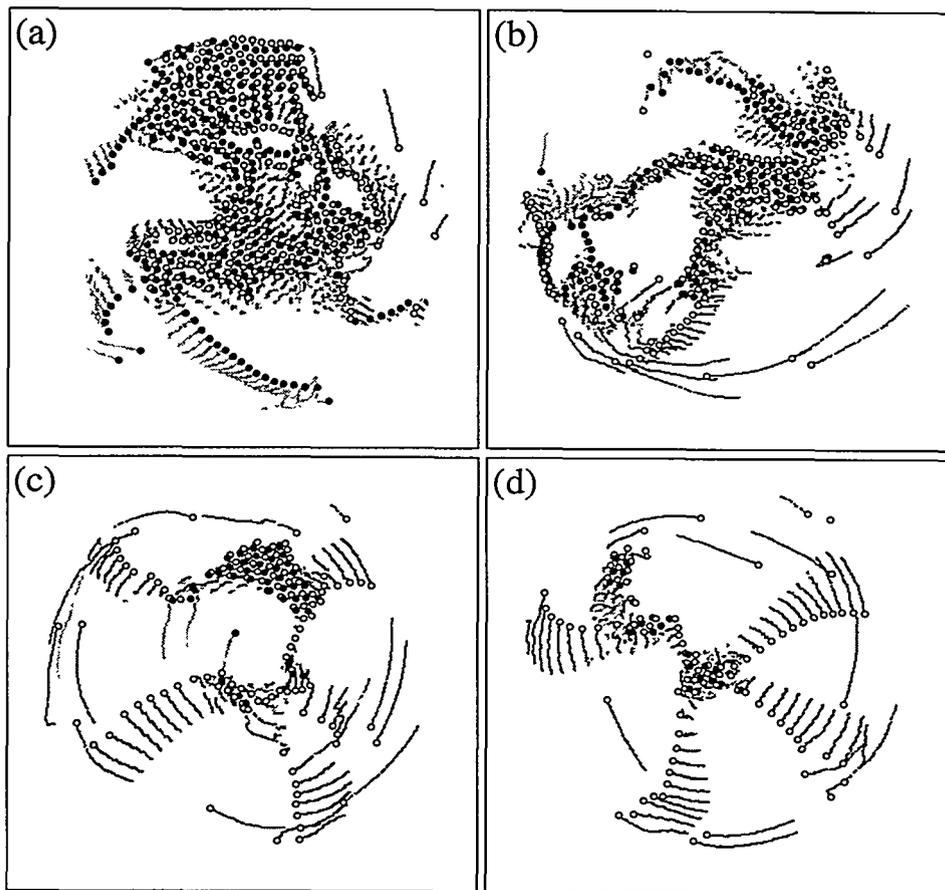

Fig. 5. Defect representation of the four patterns shown in Fig. 3. Defects of positive (negative) charge are marked by filled (open) circles. The positions of positive (negative) defects over the previous 23t are shaded in light (dark) gray.

V. PREDICTING PATTERNS AND DYNAMICS USING PHASE DEFECTS

Motivated by the experimental results on the phase defects, we considered a simple model of the patterns consisting of the arrangement of phase defects within the cell and those that describe the termination of the rolls at the cell boundary. We use the location and charges of the defects to reconstruct the patterns that are observed. The complex amplitude of a defect at (u, v) is

$$A_{u,v}(\mathbf{x}) = a(r)e^{i(c\theta + pr)}, \tag{1}$$

where c is the topological charge, θ and r are the polar coordinates about the point (u, v), and $a(r)$ is an envelope function that goes to zero as $r \to 0$. We found it necessary to include the pitch, p,

which is a radial wave number that gives the phase a spiral-shaped appearance. The pattern as a whole is given by

$$A(\mathbf{x}) = \prod_{u,v} A_{u,v}(\mathbf{x}), \qquad (2)$$

which is just the sum of the phases of each defect, either in the pattern or at the domain boundary, where the roll pairs terminate.[17] Fig. 6 compares an actual pattern, the corresponding array of defects, and the pattern reconstructed using the above formalism and a non-zero pitch. A value of $p = 0.01h^{-1}$ was found to be necessary, so that the orientation of waves near domain boundaries matches that of the observed pattern. For $p = 0$, waves make approximately equal angles to domain boundaries, instead of the angles of 0° and 90° that are observed. The remaining differences between the patterns predicted and observed are due mainly to the fact that the wave number of the experimental patterns is very rigid, with k varying less than ±10% across the convection cell. As illustrated by the right-hand panel in Fig. 6, wave number rigidity is not contained in the point defect model. Thus, an additional (and at this point unspecified) mechanism, such as phase diffusion, will be necessary to keep the wave number constant.[18] With this caveat, the arrangement of point defects describes the patterns relatively accurately.
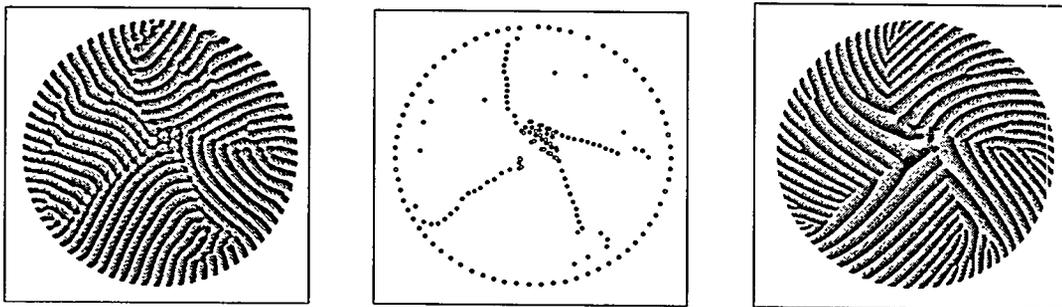

Fig. 6. The phase of the complex amplitude of a mature TW pattern is shown on the left. In the center, defects of positive (negative) topological charge for this pattern are denoted by open (filled) circles. The reconstruction of the pattern based on these defects and using $p=-0.01h^{-1}$ is shown on the right.

We have begun to consider what determines the *motion* of the defects as a way to address the dynamics of the patterns. We developed a technique to measure the phase field upon which the defects are superimposed. Using this technique, we find that we are able to correlate the defect velocity, $\mathbf{v_d}$, with the magnitude and direction of the gradient in this phase at the defect, which we denote by the wave vector $\mathbf{k_d}$. The resulting expression is

$$\mathbf{v_d} \approx \xi\mathbf{k_d} + \eta c(\mathbf{k_d} \times \mathbf{z}), \qquad (3)$$

where ξ and η are constants and c is the topological charge of the defect. The second term in the equation differs from that which would be expected in stationary convection. In that case, climb of a dislocation is a mechanism for wave number selection, and the motion of dislocations in the roll direction is proportional to $\mathbf{k_d} - \mathbf{k_0}$, where $\mathbf{k_0}$ is the preferred wave number of the pattern.

56

VI. CONCLUDING REMARKS

The phase defect description of traveling wave patterns appears to be a promising approach to describing traveling-wave patterns and dynamics. The key to this research is that convection in mixtures is a model system for studying phase turbulence -- one in which the order parameter can be measured with sufficient precision to identify and track the phase defects accurately. We have tried to determine the extent to which the traveling-wave patterns and their dynamics can be described solely in terms of the phase defects. We are now focusing on questions regarding defect motion. One open question is what determines the parameters ξ and η in Eq. 3. Our first intuition is that η could be related to the circular geometry of the convection cell, and in particular, to the curvature of the cell walls (e.g., perhaps due to mean flows). A second question is what determines the pitch, p, of the defects. We plan to pursue these topics in future experiments.

VII. ACKNOWLEDGEMENT

REFERENCES

*   Present address: Laboratory of Atomic and Solid State Physics, Cornell University, Ithaca NY 14853

1   E. N. Lorenz, J. Atmos. Sci. **20**, 230 (1963).

2   J. Murray, *Nonlinear Differential Equation Models in Biology*, Clarendon Press (1997).

3   R. E. Ecke, Y. Hu, R. Mainieri, *et al.*, Science **269**, 1704-7 (1995).

4   G. W. Baxter, R. P. Behringer, T. Fagert, *et al.*, Phys. Rev. Lett. **62**, 2825 (1989).

5   P. Coullet, L. Gil, and F. Rocca, Optics Comm. **73**, 403-8 (1989).

6   J. Lega, J. V. Maloney, and A. C. Newell, Phys. Rev. Lett. **73**, 2978-81 (1994).

7   E. Pampaloni, P. L. Ramazza, S. Residori, *et al.*, Phys. Rev. Lett. **74**, 258-61 (1994).

8   M. C. Cross and P. C. Hohenberg, Rev. Mod. Phys. **65** (1993).

9   P. Manneville, *Dissipative Structures and Weak Turbulence*, Academic Press (1990).

10   R. W. Walden, P. Kolodner, A. Passner, *et al.*, Phys. Rev. Lett. **55** (1985).

11   W. Barten, M. Lücke, W. Hort, *et al.*, Phys. Rev. Lett. **63**, 376-79 (1989).

12   A. La Porta and C. M. Surko, Phys. Rev. E **53**, 5916-34 (1996).

13   A. La Porta and C. M. Surko, Phys. Rev. E **56**, 5351-66 (1997).

14   A. La Porta and C. M. Surko, Phys. Rev. Lett. **77**, 2678-81 (1996).

15   P. Kolodner, M. Williams, and C. Moe, J. Chem. Phys. **88**, 6512 (1988).

16   A. C. Newell, T. Passot, and J. Lega, Ann. Rev. Fluid Mech. **25**, 399 (1993).

17   A. La Porta and C. M. Surko, Phys. Rev. Lett. **80**, 3759-62 (1998).

18   G. D. Granzow and H. Reicke, Physica A **249**, 27-35 (1998).

SPATIOTEMPORAL PATTERNS IN VERTICALLY VIBRATED GRANULAR LAYERS: EXPERIMENT AND SIMULATION

M. D. Shattuck, C. Bizon, J. B. Swift and Harry L. Swinney

Center for Nonlinear Dynamics
and Department of Physics
The University of Texas at Austin
Austin, TX 78712

ABSTRACT

Thin layers of vertically vibrated granular media lose stability to sub-harmonic standing wave patterns when the driving acceleration is increased above a critical value of about 2.5 times gravity. Space filling patterns, squares, stripes, and hexagons are observed for different values of the two control parameters, frequency and acceleration. Localized structures (*oscillons*), are also observed for a small range of control parameters. Event driven molecular dynamics simulations reproduce all of the space filling patterns at the same control parameters as in the experiments, and yield the pattern wavelength as a function of driving frequency to within a few percent. The simulation allows many important properties of granular flows to be determined which are difficult or impossible to measure in laboratory experiments, such as, velocity distribution functions, velocity fields, and the granular temperature. It offers a first step toward verification of rigorous theories of granular flows based on kinetic theory.

INTRODUCTION

Transport and processing of granular materials is important in industries ranging from food preparation to pharmaceuticals to coal processing. However, theoretical understanding of granular flows has lagged significantly behind liquid and gas flows. No basic theory of granular flows comparable to the Navier-Stokes equations for fluids has attained widespread acceptance[1], and it has been argued that such a theory is not possible[2]. This lack of understanding leads to significant waste in solids processing. One study found that in commercial processing plants with solid feed stock the average operating capacity was 64% of design capacity, compared with an industry standard of 90 to 95% of design capacity for plants with liquid or gas feed stock[3]. An increased understanding of granular flows could improve this situation. The goal of our current research in granular materials is to elucidate and test basic granular theories with high precision experiments and molecular dynamics simulations.

Recent experiments[4, 5, 6] show pattern formation in vertically vibrated granular layers which is strikingly similar to patterns seen in fluid systems (see Figure 1). This similarity suggests that

in this system, equations of motion similar to Navier-Stokes could be found. Equations similar to Navier-Stokes have been derived from kinetic theory for granular media flows under the assumption of binary hard sphere collisions and in the limit of small energy loss in collisions[7, 8, 9, 10, 11, 12]. These theories produce equations that differ slightly from the dense gas Navier-Stokes equations by the addition of a temperature loss rate term in the energy equation, in the form of the constitutive relations for shear and bulk viscosity and thermal conductivity, and in the equation of state for the pressure. In these equations the granular temperature is not the thermodynamic temperature but by analogy to molecular gases is the average of the square of the deviations of the velocity from the mean velocity (i.e., the variance of the velocity). While these equations have been available for 25 years there have been few experimental[13, 14, 15] or numerical[16, 17, 18, 19] tests. This deficiency may be due to the fact that many granular flows do not show obvious fluid-like behaviors because inelasticity of the particle collisions drives the granular temperature very low.

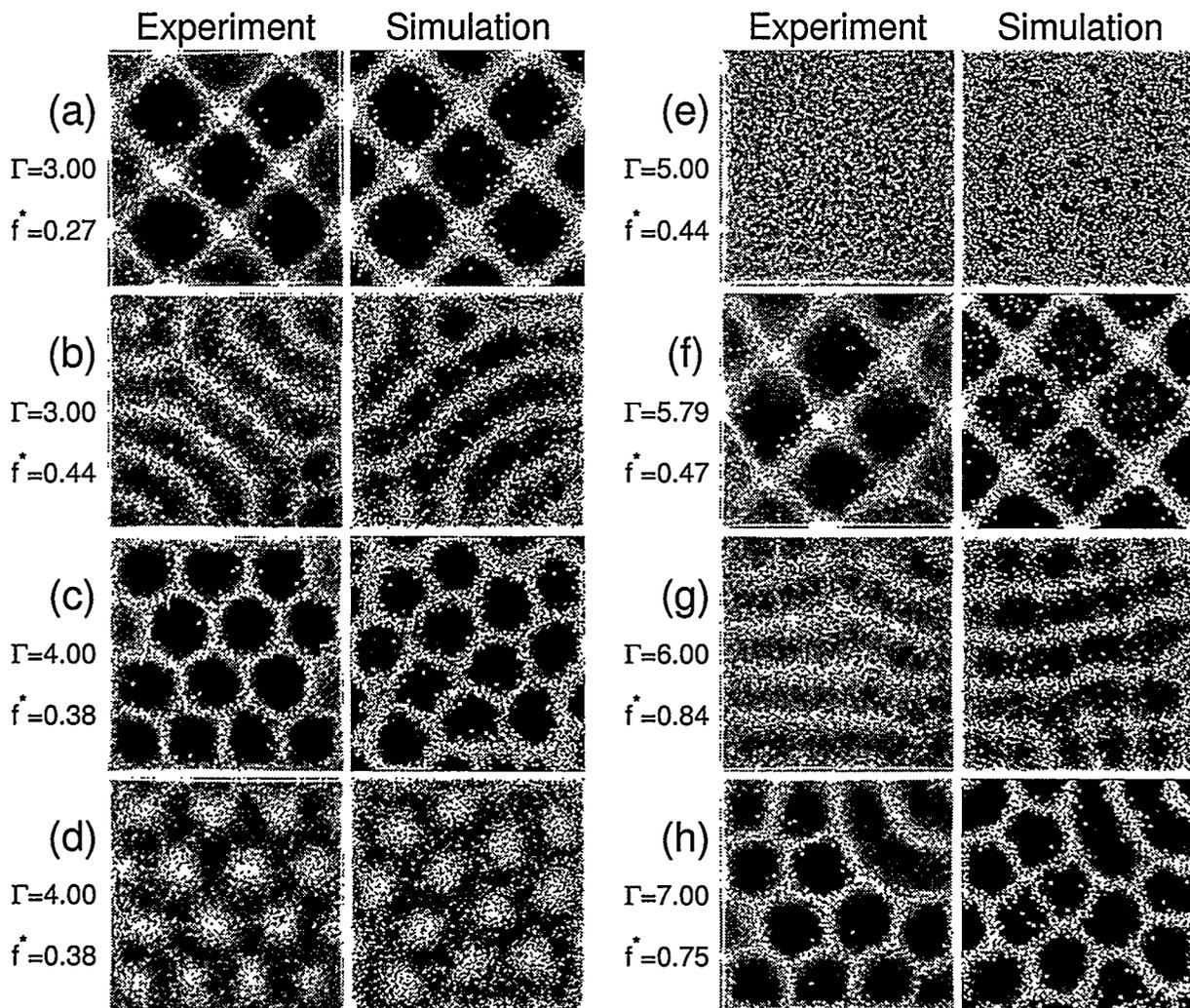*Figure 1.* Comparison of standing wave patterns obtained in experiment and simulation: (a) squares, (b) stripes, (c) and (d) alternating phases of hexagons, (e) flat, (f) squares, (g) stripes, (h) hexagons. (a)–(e) oscillate at $f/2$ and (f)-(h) oscillate at $f/4$. The layer depth is 5.42 particle diameters. The experiments use lead spheres sieved between 0.5 and 0.6 mm in a container which is 100 particle diameters on each side.

Experiments in vibrated layers of granular materials provide an unprecedented opportunity to study granular fluid-like behavior. However, experiments alone do not provide information on the microscopic underpinnings of the kinetic theory description, due to the difficulty of internal measurements in three dimensional systems. To overcome this difficulty we have developed an event driven molecular dynamics simulation capable of quantitatively reproducing our experiments[20], including wavelength changing secondary instabilities[21]. The simulation is based on assumptions similar to those for granular kinetic theory. In particular, particles obey Newton's laws between binary instantaneous collisions (hard sphere model) which conserve momentum, but dissipate energy. However, unlike the kinetic theory models the energy dissipation can be large. Using this simulation we have also found enhanced diffusion perpendicular to the stripe patterns and internal convection rolls in all of the pattern states[22].
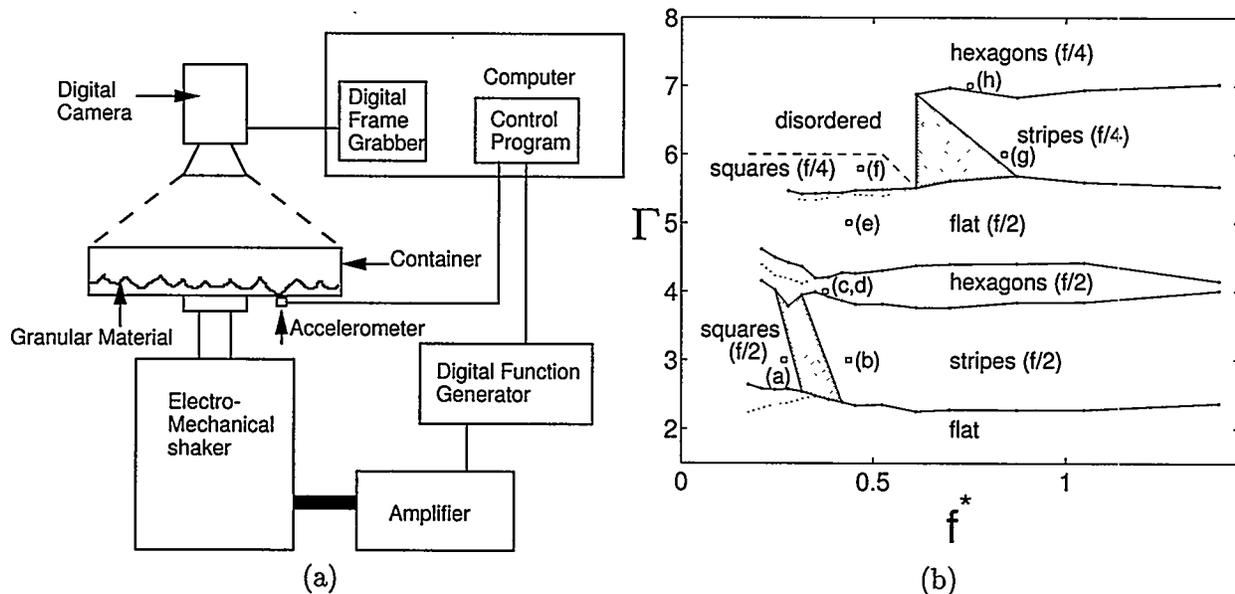
Digital Camera

Computer
Digital Frame Grabber
Control Program

Container

Granular Material

Accelerometer

Electro-Mechanical shaker

Digital Function Generator

Amplifier

(a)

8

7

6

Γ 5

4

3

2

hexagons (f/4)
□(h)
disordered
stripes (f/4)
squares (f/4) □(f)
□(g)
□(e)   flat (f/2)
□(c,d)   hexagons (f/2)
squares (f/2) □
□(b)   stripes (f/2)
(a)
flat

0   0.5   1

f *

(b)

Figure 2. (a) Schematic of the experimental apparatus showing the container, the shaker and the imaging system. The camera can be placed above, to produce images like those in Figure 1, or to the side of the test cell, to produce images like those in the top of Figure 3(b). Phase diagram from the experiments for layer depth of 5.71 particles. The parameter values used for the patterns in Figure 1 are indicated by (a) through (h). Solid lines denote the transitions with increasing Γ, and dotted lines denote transitions for decreasing Γ. Shaded areas show transitional regions between stripes and squares.

EXPERIMENTAL APPARATUS

The experiment consists of an evacuated container filled with a thin layer of particles (2–30 particle diameters deep) and vibrated sinusoidally $(A\sin(2\pi f t))$ in the vertical direction by an industrial electro-mechanical shaker (see Figure 2(a)). Evacuation eliminates a heaping instability caused by interaction of the grains with the interstitial gas[23]. The top and sides of the container are transparent for visualization by a high speed digital camera and the bottom is aluminum. Many different types of particles (e.g., bronze, lead, glass, plastic, rice, etc.) and diameters (0.05–3 mm) have been used and produce qualitatively similar results. The control parameters are the acceleration amplitude A, varied up to 1 cm, and the frequency f, varied from 10 to 200 Hz. Experiments are typically performed at constant $\Gamma = 2\pi A f^2/g$, where g is the gravitational acceleration constant, and f is

60

varied. A computer stores digital images and controls the acceleration amplitude using feedback from an accelerometer.
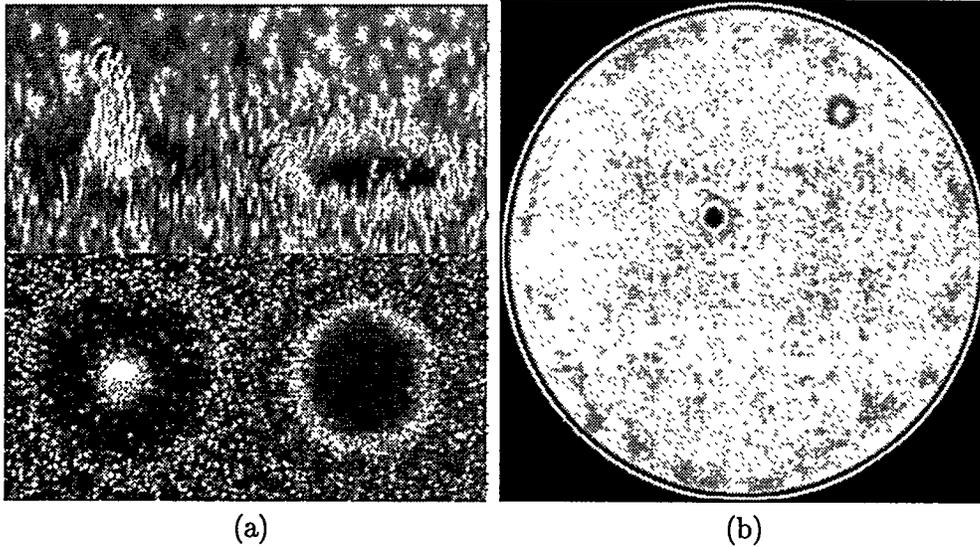

(a)   (b)

Figure 3.   (a) Side and top views of single oscillons. The left and right images are separated by one container oscillation. (b) Oscillons observed using 0.15–0.18 mm bronze spheres, 17 particle diameters deep in a 126 mm cell at $f = 26$ Hz and $\Gamma = 2.54$.

PATTERNS

When the layer is oscillated at an acceleration amplitude below $\Gamma = 1$, it remains stationary in the reference frame of the container. For $\Gamma_c > \Gamma > 1$, the layer leaves the bottom plate of the cell for a portion of the cycle, but the top and bottom surfaces of the layer remain flat until a critical acceleration Γ_c is reached and the flat layer becomes unstable to spatially periodic standing waves, which oscillate at $f/2$ [4]. Particles alternately form peaks and valleys through a horizontal sloshing motion driven by collision with the plate. As the acceleration is increased further, a bifurcation sequence is observed which is summarized in Figure 2(b). The patterns show some hysteresis in Γ at low frequencies where the pattern is squares (Figure 1(a)). At higher frequencies the pattern is stripes (Figure 1(b)). If Γ is increased further to about 4, both squares and stripes lose stability to hexagonal patterns (Figure 1(c,d)). At still larger Γ the layer is thrown so high that it impacts the plate only once every other oscillation and hexagons become unstable to a flat layer (Figure 1(e)) which oscillates at $f/2$. Because the layer oscillates at $f/2$, two phases with respect to the driving frequency can co-exist in the container forming a kink between the regions of different phase. Further increases in Γ cause the sequence of bifurcations to be repeated, except now the pattern oscillates at $f/4$. From $\Gamma = 7$ to 10 (the largest Γ studied) a disordered state exists. Much of this phase diagram can be explained using a simple model which treats the layer as a single totally inelastic ball[5].

In a small strip of the phase diagram in deep layer (> 13 particle diameters), localized structures (*oscillons*) form (Figure 3) as Γ is lowered below the point where squares are stable. The strip is about 2% of Γ_c tall and 15 Hz long for a layer of 0.15–0.18 mm bronze spheres at a depth of 19 particle diameters. Oscillons are stable localized structures oscillating at $f/2$, just like the standing wave patterns described above. Figure 3(b) shows two oscillons in a 126 mm diameter cell. Due to the sub-harmonic nature of this pattern, two phases of oscillons can coexist as can be seen in the figure. Figure 3(a) shows close up side and top views of an oscillon at each phase. Oscillons of unlike

phase can bind to form pairs, chains, and other complex structures with coordination number up to three [6].
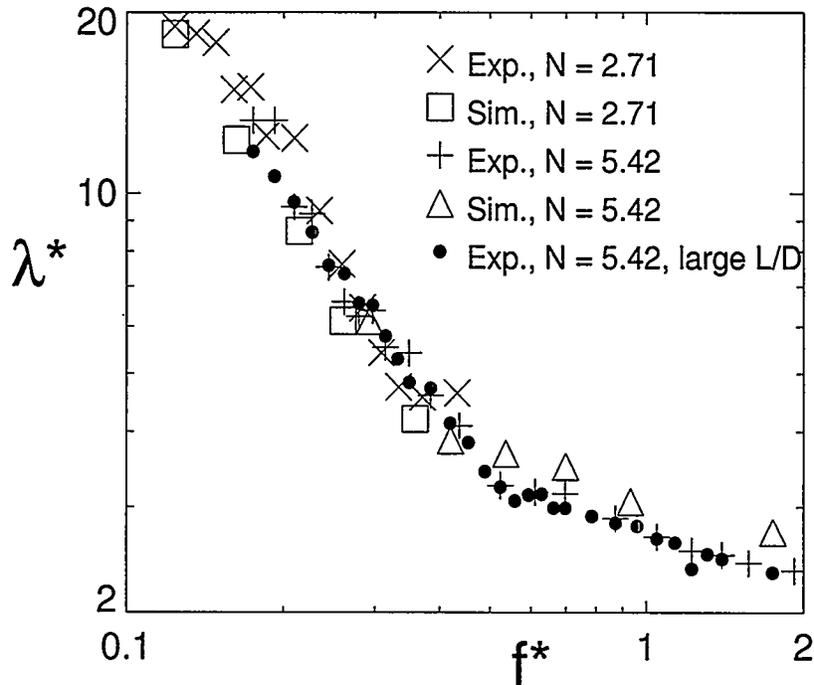
(b)

Figure 4. Wavelength vs. frequency from simulations and experiments with $\Gamma = 3.0$. The + and × points are obtained from experiments with lead spheres ($D = 0.55$ mm) in a container 100 particles on each side, while the • points correspond to experiments with bronze spheres ($D = 0.165$ mm) in a container with a diameter L of 982 particles.

NUMERICAL SIMULATION

We have developed an event driven numerical simulation to model the system described above[20]. In this type of simulation[24, 25] time advances from collision to collision with ballistic motion between collisions. A sorted list of the time-to-next-collision for each particle is used to determine when the next collision will occur. The simulation advances through the collision using a model which maps the velocities and angular velocities of each particle before the collision to their values after the collision. Collisions conserve linear and angular momentum, but not energy. The collision duration is assumed zero, therefore limiting the particle interactions to binary collisions. Energy is lost in collisions though a normal coefficient of restitution e defined by the ratio of the outgoing normal relative velocity and the incoming normal relative velocity. Therefore energy is lost at a rate of $1 - e^2$ per collision. Interactions with the four walls and the bottom plate are treated like particle-particle interactions in which one particle's (i.e., the wall's) mass goes to infinity. For comparison with simulation a special cell was constructed to match as closely as possible the conditions of the simulation. Either $60,000 \pm 8$ or $30,000 \pm 8$ lead spheres corresponding to layer depths of $H = 5.42$ and $H = 2.71$ particle diameters respectively were oscillated in a square container 100 particle diameters wide. The particles were sieved between 0.5 mm and 0.6 mm. Experiments and simulation are compared using a non-dimensional frequency $f^* = f\sqrt{H/g}$.

62

Three collisional particle properties — the coefficient of friction μ, the normal coefficient of restitution e, and the cutoff for the rotation coefficient of restitution β_0 — must be determined for the simulation. β_0 is taken from the literature[26]. e and μ are determined by adjusting their values until the pattern wavelength in the simulation and experiment matched in two specific runs, $\Gamma = 3.0$, $f^* = 0.205$, $H = 2.71$ (for e), and $\Gamma = 3.0$, $f^* = 0.534$, $H = 5.42$ (for μ). By this procedure the value of e is set to 0.7 and μ to 0.5. However, the values of these parameters do not strongly effect the qualitative behavior of the simulation, only the quantitative agreement. For example, a change in e from 0.5 to 0.8 only changes the observed wavelength of the pattern by 30%, the pattern planform is not effected.

The results of the simulation for various control parameters are shown in Figure 1. Patterns are obtained in the simulation and experiment at the same values of control parameters which are denoted by points on the phase diagram (Figure 2(b)) labeled (a)–(h). Both $f/2$ (a)–(e) and $f/4$ (f)–(h) patterns show a striking correspondence. Further, the pattern wavelengths for various f^*, in experiment and simulation agree well, even when comparing the simulation in a cell 100 particle diameters wide with experiments in a large container with a diameter of 982 particle diameters (Figure 4).

Currently, simulations have not reproduced stable oscillons. However due to the extremely small range of stability and the layer depths required, this is not surprising. The computational time depends of the square of the depth, which makes the search intractable with the current code.

DISCUSSION

Using this simulation we have also determined properties of the vibrated granular system which can not be easily measured in the experiment. For example we have found enhanced diffusion of particles perpendicular to the stripe pattern direction (i.e., from peak to peak), and discovered a convective roll pattern within each peak and valley of the pattern[22]. The convective roll pattern is a prediction of the simulation, but has not been verified experimentally. Anisotropic diffusion is also seen in other fluid systems as a result of advection (e.g., Rayleigh-Bénard convection).

de Bruyn et al.[21] describe another similarity of granular pattern formation to Rayleigh-Bénard convection. Wavelength changing secondary instabilities define a wavenumber stability region between cross-roll and skew-varicose instabilities. Event driven simulations show the same instabilities and allow the calculation of average vertical vorticity which is shown to be large only during a skew-varicose instability just as in the fluid case[21].

The good agreement between simulation and experiment validates the assumptions of the simulation model. The basic assumptions of the model are that particles follow Newton's law between collisions, and collisions are binary, conserve momentum, and dissipate energy. These are the same assumptions of granular kinetic theory[7, 8, 9, 10, 11, 12], with the addition that the energy loss and density are small and that there are no velocity correlation. To further test the ideas of granular kinetic theory we have performed two-dimensional simulations of a granular gas of inelastic hard disks, driven uniformly by a heat bath[18, 19]. This system was chosen as our first test because direct comparison with the transport coefficients can be made with the values calculated analytically from granular kinetic theory. We find that although velocity correlations do exist[19] granular kinetic theory describes the system well even for strong dissipation, high densities, and small numbers of particles[18]. Specifically, for $e = 0.7$, which corresponds to about half of the energy lost per collision, densities up to 0.75 volume fraction, and a system size of 52.6 particle diameters, the energy loss rate and the shear viscosity deviate by less than 20%, and the thermal conductivity deviates by less than 50%. For all transport coefficients, the deviation from kinetic theory improves if dissipation and density are decreased, in accord with the assumption that they are small. The general level of agreement is surprisingly good considering that the density and energy loss per

collision is so high, and suggests that a continuum approach may be able to quantitatively as well as qualitatively describe some granular systems.

ACKNOWLEDGEMENTS

REFERENCES

1. H. M. JAEGER, S. R. NAGEL, and R. P. BEHRINGER, "The Physics of Granular Material," *Physics Today*, 49 32–38 (1996).

2. L. P. KADANOFF, "Built Upon Sand: Theoretical Ideas Inspired by the Flow of Granular Materials," *Rev. Mod. Phys.*, 71 435–444 (1999).

3. E. W. MERROW, "Linking R&D to Problems Experienced in Solids Processing," *Chem. Eng. Progress*, 81 14 (1985).

4. F. MELO, P. UMBANHOWAR, and H. L. SWINNEY, "Transition to Parametric Wave Patterns in a Vertically Oscillated Granular Layer," *Phys. Rev. Lett.*, 72 172–175 (1994).

5. F. MELO, P. B. UMBANHOWAR, and H. L. SWINNEY, "Hexagons, Kinks, and Disorder in Oscillated Granular Layers," *Phys. Rev. Lett.*, 75 3838–3841 (1995).

6. P. UMBANHOWAR, F. MELO, and H. L. SWINNEY, "Localized Excitations in a Vertically Vibrated Granular Layer," *Nature*, 382 793–796 (1996).

7. J. T. JENKINS and M. W. RICHMAN, "Grad's 13-moment system for a dense gas of inelastic particles," *Arch. Rat. Mech. Anal.*, 87 355–377 (1985).

8. J. T. JENKINS and S. B. SAVAGE, "A theory for the rapid flow of identical, smooth, nearly elastic particles," *J. Fluid Mech.*, 130 187–202 (1983).

9. C. K. K. LUN, S. B. SAVAGE, D. J. JEFFREY, and N. CHEPURNIY, "Kinetic theories for granular flow: inelastic particles in Couette flow and slightly inelastic particles in a general flowfield," *J. Fluid Mech.*, 140 223–56 (1983).

10. C. K. K. LUN and S. B. SAVAGE, "The effects of an impact velocity dependent coefficient of restitution on stresses devloped by sheared granular materials," *Acta Mechanica*, 63 15–44 (1986).

11. C. K. K. LUN, "Kinetic theory for granular flow of dense, slightly inelastic, slightly rough spheres," *J. Fluid Mech.*, 233 539–559 (1991).

12. A. GOLDSHTEIN and M. SHAPIRO, "Mechanics of Collisional Motion of Granular Materials. Part 1. Gene ral hydrodynamic equations," *J. Fluid Mech.*, 282 75–114 (1995).

13. T. G. DRAKE, "Granular flow: physical experiments and their implications for microstructural theories.," *J. Fluid Mech.*, 225 121–152 (1991).

14. J. DELOUR, A. KUDROLLI, and J. P. GOLLUB, "Velocity distributions in vertically vibrated granular media," *preprint* (1998).

15. J. S. OLAFSEN and J. S. URBACH, "Clustering, order, and collapse in a driven granular monolayer," *Phys. Rev. Lett.*, 81 4369–72 (1998).

16. C. S. CAMPBELL, "Rapid Granular Flows," *Annu. Rev. Fluid Mech.*, 2 57–92 (1990).

17. E. L. GROSSMAN, T. ZHOU, and E. BEN-NAIM, "Towards granular hydrodynamics in two dimensions," *Phys. Rev. E*, 55 4200 (1997).

18. C. BIZON, M. D. SHATTUCK, J. B. SWIFT, and H. L. SWINNEY, "Transport Coefficients for Granular Media from Molecular Dynamics Simulations," *Submitted to Phys. Rev. E* (1999).

19. C. BIZON, M. D. SHATTUCK, J. B. SWIFT, and H. L. SWINNEY, "Velocity correlations in driven two-dimensional granular media," In *Dynamics: Models and Kinetic Methods for Nonequilibrium Many-Body Systems*, J. KARKHECK, ed., NATO ASI Series E: Applied Sciences (Kluwer Academic publishers, Dordrecht, 1999).

20. C. BIZON, M. D. SHATTUCK, J. B. SWIFT, W. D. MCCORMICK, and H. L. SWINNEY, "Patterns in 3D Vertically Oscillated Granular layers: Simulation and Experiment," *Phys. Rev. Lett.*, 80 57–61 (1998).

21. J. R. DE BRUYN, C. BIZON, M. D. SHATTUCK, D. GOLDMAN, J. B. SWIFT, and H. L. SWINNEY, "Continuum-type stability balloon in oscillated granular layers," *Phys. Rev. Lett.*, 81 1421–1424 (1998).

22. C. BIZON, M. D. SHATTUCK, J. R. DE BRUYN, J. B. SWIFT, W. D. MCCORMICK, and H. L. SWINNEY, "Convection and Diffusion in Vertically Vibrated Granular Paterns," *J. Stat. Phys.*, 93 449 (1998), Color pictures of granular convection can be found at http://chaos.ph.utexas.edu/errata/bizon98a.html.

23. H. K. PAK, E. VAN DOORN, and R. P. BEHRINGER, "Effects of Gases on Granular Materials under Vertical Vibration," *Phys. Rev. Lett.*, 74 4643–4646 (1995).

24. M. MARíN, D. RISSO, and P. CORDERO, "Efficient Algorithms for Many-Body Hard Particle Molecular Dynamics," *J. Comput. Phys.*, 109 306–317 (1993).

25. B. D. LUBACHEVSKY, "How to Simulate Billiards and Similar Systems," *J. Comp. Phys.*, 94 255–283 (1991).

26. O. R. WALTON, "Numerical Simulation of Inelastic, Frictional Particle-Particle Interactions," in *Particulate Two-Phase Flow*, M. C. ROCO, ed., (Butterworth-Heinemann, Boston, 1993), pp. 884–911.